

Hsp90 Induces Acsl4-dependent Glioma Ferroptosis via Dephosphorylate Ser637 at Drp1

Ning Liu (✉ liuning0853@126.com)

Nanjing Medical University <https://orcid.org/0000-0001-7895-1285>

Zong Miao

Nanjing Medical University

Wei Tian

Nanjing Medical University

Zhongyuan Bao

Nanjing Medical University

Guangchi Sun

Nanjing Medical University

Lei Xu

Nanjing Medical University

Chong Li

Nanjing Medical University

Yangfan Ye

Nanjing Medical University

Yiming Tu

Nanjing Medical University

honglu Chao

Nanjing Medical University

Sin Man Lam

National Lipid Association

Jing Ji

Nanjing Medical University

Research Article

Keywords: Glioma, Ferroptosis, Acsl4, Drp1, Hsp90

Posted Date: January 13th, 2022

DOI: <https://doi.org/10.21203/rs.3.rs-1131699/v1>

License:  This work is licensed under a Creative Commons Attribution 4.0 International License.

[Read Full License](#)

Abstract

Background: Ferroptosis is a newly identified form of regulated cell death (RCD) characterized by the iron-dependent lipid reactive oxygen species (ROS) accumulation, but its exact mechanism in gliomas remains elusive. Acyl-coenzyme A (CoA) synthetase long-chain family member 4 (Acsl4), a pivotal enzyme in the regulation of lipid biosynthesis, has been found to benefit the initiation of ferroptosis, but its role in gliomas likewise needs clarification. Erastin, widely investigated as an inducer of ferroptosis, was recently found to regulate lipid peroxidation by regulating Acsl4 other than glutathione peroxidase 4 (GPX4) in ferroptosis.

Methods: Relationship between Hsp90, Drp1 and Acsl4 was determined by Co-immunoprecipitation/Mass spectrometry and western blot assay. The impact of Hsp90 and Drp1 on Acsl4-dependent ferroptosis was examined by lipid peroxidation indicators in patient-derived PL1 and PG7 cells. The morphological changes of mitochondria are observed by confocal-fluorescence microscopy and transmission electron microscope. Therapeutic efficacy of Erastin-induced ferroptosis *in vivo* was examined in xenograft mouse models.

Results: In this study, we demonstrated that heat shock protein 90 (Hsp90) and dynamin-related protein 1 (Drp1) actively regulated Acsl4 expression in erastin-induced ferroptosis in gliomas. Hsp90 overexpression and calcineurin (CN)-mediated Drp1 dephosphorylation at serine 637 (Ser637) promoted ferroptosis by altering mitochondrial morphology and increasing Acsl4-mediated lipid peroxidation. Importantly, the Hsp90-Acsl4 pathway mediated Acsl4-dependent ferroptosis, amplifying the anticancer activity of erastin *in vitro* and *in vivo*.

Conclusions: Our study not only uncovered an important role of Hsp90-Drp1-Acsl4 pathway in erastin-induced ferroptosis but also reveals an efficient mechanism of Acsl4 as a potential therapeutic target to ferroptosis-mediated glioma therapy.

Background

Glioma, the most common type of malignant intracranial tumor, is characterized by aggressiveness and recurrence[1]. Treatment regimens including surgery, radiotherapy and chemotherapy have been used, based on differing grades of glioma[2]. Although improvements have been made in the treatment of this cancer, patient survival rates are low and prognoses poor due to therapeutic resistance. Thus, exploring new therapeutic agents is urgently needed for the treatment of glioma.

Ferroptosis, is a recently recognized form of iron-dependent and Caspase-independent cell death[3]. It is distinct from other classical types of non-apoptotic cell death, including necrosis and apoptosis, by its biochemical characteristics of iron and lethal-lipid reactive oxygen species (ROS) accumulation, involvement of an individual set of genes, and mitochondrial-morphology shrinkage with condensed mitochondrial-membrane densities[4, 5]. The biochemical mechanism underlying ferroptosis is peroxidation of phospholipids (PLs) that contain polyunsaturated fatty acids (PUFAs), most notably

arachidonic acid (AA) and adrenic acid (AdA)[6, 7]. Recent studies have implicated ferroptosis in several pathophysiological contexts, such as renal failure, intestinal ischemia/reperfusion (I/R), and tumors[8, 9, 10]. In addition, cancer cells that have a high tendency to metastasize or show resistance to conventional therapies might be particularly sensitive to ferroptosis[11]. Therefore, it has been suggested to be promising for cancer therapeutics. Erastin, which differs from other ferroptosis inducers such as *Ras*-selective lethal small-molecule 3 (RSL3) and sorafenib, can induce ferroptosis by triggering multiple pathways and has been shown to exert effects in cancer therapy[4, 12].

Acyl-coenzyme A (CoA) synthetase long-chain family member 4 (Acsl4) is a member of the long-chain acyl CoA synthase (ACSL) family that has been found to be a crucial factor in fatty-acid metabolism[13]. Ferroptosis is biochemically characterized by lipid peroxidation, which mainly involves preferential oxidation of polyunsaturated fatty acids (PUFAs) such as arachidonic acid (AA) and adrenic acid (AdA) [14, 15]. Recently, Acsl4 was shown to catalyze the esterification of arachidonoyl and adrenoyl into phosphatidylethanolamine (PE)[16]. Moreover, Acsl4-mediated production of 12- and 15-hydroxyeicosatetraenoic acids (12-HETE, 15-HETE) is essential for ferroptosis[17]. Therefore, Acsl4 has been identified as a vital component of the process of ferroptosis, as well as a predictive marker of ferroptosis sensitivity in different types of cells. Hitherto, Acsl4 has rarely been mentioned in gliomas. Therefore, further understanding of its functional role and interaction with ferroptosis is needed in relation to this cancer.

In this study, we demonstrated that Acsl4 was highly inducible following erastin treatment of glioma cells. Upregulation of the heat shock protein 90 (Hsp90)-dynamin-related protein 1 (Drp1)-Acsl4 pathway actively regulated ferroptosis via accumulation of lipid ROS and changes in mitochondrial morphology. Genetic inhibition of the Hsp90-Drp1-Acsl4 pathway *in vitro* and *in vivo* diminished the anticancer activity of erastin-induced ferroptosis. Our findings suggest that Acsl4 could play a unique role in the regulation of ferroptosis, particularly in erastin-mediated anticancer therapy. Collectively, we intend to provide a new perspective and target in glioma treatment.

Methods And Materials

Isolation and culture of cells

The four low-grade glioma (LGG) and seven glioblastoma (GBM) specimens were derived from excess surgical materials of patients (Supplementary. Table. S1). All the patients had signed informed consent and were enrolled according to the institutional protocols (Ethics number:2019-SR-479) by the Ethics Committee of the First Affiliated Hospital of Nanjing Medical University. Patient-derived PL1 and PG7 cells were obtained from primary patient brain tumor specimens. Described briefly, divided tumor tissues were digested with 0.1% trypsin (Invitrogen, USA) and DNase I (Promega, USA) for 1 h at 37°C. Erythrocytes were lysed using Red Blood Cell Lysis Buffer (Beyotime, C3702, Shanghai, China). After being washed twice with PBS, the tissues were triturated by pipetting and passed through a 100 µm cell filter.

PL1 and PG7 cells were cultured in DMEM containing 10% fetal bovine serum (Gibco, USA) at 37°C with 5% CO₂.

Western blot

After extraction, proteins in cell lysates were first resolved by sodium dodecyl sulfate polyacrylamide gel electrophoresis (SDS-PAGE) and then transferred to nitrocellulose membrane, which was subsequently blocked with 6% nonfat dry milk in TBST for 2 h and incubated with the primary antibody. Antibodies used for western blot analysis were Acsl4 (ab155282), Drp1 (ab184247), and Hsp90 (ab59459) from Abcam; Calcineurin (CST2614), p-Drp1^{Ser637} (CST4867S), and p-Drp1^{Ser616} (CST-3455S) from Cell Signaling Technology; and GAPDH (sc137179) from Invitrogen. After incubation with peroxidase-conjugated secondary antibodies, the signals were probed using the SuperSignal® Maximum Sensitivity Substrate (Thermo Fisher Scientific). The relative band intensity was analyzed using the Image Lab software (Bio-Rad).

Immunohistochemistry (IHC) assay

Human glioma biopsy specimens and human xenograft mice tumors were fixed with 4% paraformaldehyde, then processed into 10- μ m-thick sections and immunostained with specific antibodies for Acsl4, Drp1, p-Drp1^{Ser637}, p-Drp1^{Ser616} and Ki67 (GB111141). Slides were imaged under a light microscope (Leica, Germany). Percentage of positive cells was calculated by counting under high magnification ($\times 400$).

Lipid ROS imaging and analysis

Lipid ROS imaging: Cells were planted on 6-well chamber slides (5×10^5 cells / well) for 24 h. Slides were washed with PBS and incubated with PBS containing 2 mM BODIPY 581/591 C11 (D3861, Invitrogen) and 200 nM Mito Tracker Deep Red FM (Invitrogen) for 20 min. The slides were then imaged using a confocal microscope. (Carl Zeiss Microscopy GmbH, Germany).

Lipid ROS analysis: Lipid ROS was determined using an ROS Assay Kit (Beyotime, S0033S, Shanghai, China) followed by flow cytometry and lipid peroxidation (malondialdehyde, MDA) assay (Beyotime, S0131S, Shanghai, China) according to the manufacturer's protocols.

12-HETE and 15-HETE levels were detected respectively by 12-HETE ELISA kits (ab133034, Abcam) and 15-HETE ELISA kits (ab133035, Abcam) according to the manufacturer's instructions.

GSH and GPX activity assay

Reduced glutathione (GSH) was detected by GSH and GSSG Assay Kits (Beyotime, S0053, Shanghai, China). Glutathione peroxidase (GPX) activity was determined using a Glutathione Peroxidase Assay Kit (Beyotime, S0056, Shanghai, China).

Co-immunoprecipitation and silver staining

PL1 cells were washed with pre-cold PBS and then lysed using RIPA Lysis Buffer (Beyotime, P0013D, Shanghai, China) containing protease inhibitors (PMSF). The lysate supernatants were incubated with Acsl4 antibody (ab155282), or IgG antibody (Beyotime, A0192, Shanghai, China) overnight at 4°C. The immunocomplex precipitation were formed when added with protein A/G plus agarose (sc2003) at 4°C for another 6 h. Microbeads were washed with 1x loading buffer to remove unbound proteins. Precipitated proteins were analyzed by immunoblotting. Mouse IgG was used as negative control. Silver staining was performed using a Fast Silver Stain Kit(Beyotime, P0017S, Shanghai, China) according to the manufacturer's protocol.

Immunofluorescence staining

Cells were planted on 24-well plates chamber slides and grew overnight to adhere. Dual immunostaining was performed sequentially: Cells were fixed with cooled 4% paraformaldehyde for 30 min and permeabilized with 0.25% Triton X-100 for 1 h. After being blocked with 5% BSA for 1 h, cells were incubated in 5% BSA at 4°C overnight with primary antibody. Next, cells were washed with PBS twice and incubated in 5% BSA for 1 h at room temperature with secondary antibodies Alexa Fluor 488 (Lot:12194) and Cy3(Lot:125099) from Jackson ImmunoResearch (USA). Nuclei were stained with Hoechst (Beyotime,33342,Shanghai, China). Photos were taken using a confocal microscope (Carl Zeiss Microscopy GmbH, Germany).

Flow cytometry

Cells were digested and washed twice with PBS, centrifuged at 2000 rpm for 5 min and aliquoted 3×10^5 cells in flow cytometry tubes. Cells were fixed using cold 4% paraformaldehyde for 10 min, permeabilized with 0.25% Triton X-100 for 15 min and blocked for 30 min at room temperature with 5% BSA. Cells were then immunostained in 0.1% Triton X-100 and 1% BSA at 4°C for 1 h using p-Drp1^{Ser637} (CST4867S) and p-Drp1^{Ser616} (CST-3455S) and secondary antibody Alexa Fluor 488 (Lot:12194). Labeled cells were resuspended in 300 μ L PBS and analyzed using BD LSR Fortessa™ X-2ab150077II analyzer (BD Biosciences, San Jose, CA). Data were analyzed using the FlowJo -V10.

Colony formation assay

Cells were planted in culture dishes (1×10^6 cells/dish) and cultured for two weeks. Subsequently, cells were washed with PBS, fixed with 4% formaldehyde for 10 min and stained with 0.5% crystal violet for 30 min. Colonies containing > 50 stained cells were classified as clones.

Cell viability analysis and lactate dehydrogenase (LDH) assay

Cells were seeded in a 96-well plate and cell viability was determined by Cell Counting Kit-8(CCK-8) assay (Beyotime, C0037,Shanghai, China) according to the manufacturer's instructions. The absorption was measured at 450 nm with microplate reader. LDH release was measured using an LDH Cytotoxicity Assay

Kit (Beyotime, C0016, Shanghai, China) according to the manufacturer's instructions. The absorbance was then measured at 490nm with the microplate reader.

Vectors and lentiviral transfection

The lentivirus-based plasmid shRNA of PL1 targeting Acsl4 and Hsp90, and the overexpression plasmid vector of PG7 targeting Acsl4 and Hsp90 were purchased from Genepharma (shAcsl4 target sequence: 5'-AUUGCUAUGAUGCAUCAUCAC

UCCC3', shHsp90 target sequence: 5'-CCAACTCATGTCCCTCATCAT-3'. Acsl4 overexpression vectors: forward 5'-TTTAACTTAAGCTTGGTACCATGGCAAAG

AGAATAAAAGCTAAGC-3' and reverse 5'-AACGGGCCCTCTAGACTCGAGTTA

TTTGCCCCATACATCCG-3', Hsp90 overexpression vectors: forward 5'-AGTCTC

GAGGTCACCAGAACTATGTGTTTG and reverse 5'-ATTGCGGCCGCATCTCCT

CTGTATTTATCT). The plasmids were transfected into cells using Lipofectamine 2000 (Invitrogen, Carlsbad, CA, USA) according to the manufacturer's protocol. Drp1^{S637E} and Drp1^{S637A} mutant were obtained using the QuickChange Multi III Site-Directed Mutagenesis Kit (Stratagene, North Torrey Pines, CA) and verified by sequencing. Primer sequences were as follows: Drp1^{S637E} forward: ATTCCAATTA

TGCCAGCCGAGCCACAAAAAGGTCATGCCGT and reverse : ACGGCATGAC

CTTTTTGTGGCTCGGCTGGCATAATTGGAAT; Drp1^{S637A} forward: GTTCCTGT

TGCACGAAAAGCTAGCTGCTCGGGAAC and reverse : GTTCCCGAGCAGCTA

GTTTTCGTGCAACAGGAAC.

Quantitative RT-PCR

Total RNA was extracted from PL1 and PG7 cells using TRIzol reagent (Thermo Fisher Scientific, USA) following the manufacturer's instructions. Primer sequences were as follows: Acsl4 forward: 5'-GCTACTTGCCCTTTGGCTCATGTGC -3' and reverse: 5'-GTGTGGGCTTCAGTACAGTACAGTCTCC-3'.

5-ethynyl-2'-deoxyuridine (EdU) assay

Cell proliferation was determined using an EdU Proliferation Kit (Beyotime, C0071S, Shanghai, China). Cells were cultured in a 48-well plate for 24 h, then incubated with 50 mM EdU solution for 2 h and fixed in 4% paraformaldehyde. Subsequently, the cells were permeabilized with 0.25% Triton X-100 for 15 min and sequentially stained with Alexa Fluor 488 (Lot:12194) and Hoechst (Beyotime,

33342, Shanghai, China). The EdU-treated cells were then imaged and assessed using an Olympus FSX100 microscope (Olympus, Tokyo, Japan).

Terminal deoxynucleotidyl transferase dUTP nick end labeling (TUNEL) assay

PL1 cells, PG7 cells, and xenograft tumor sections were fixed in 4% paraformaldehyde for 15 min. TUNEL staining was performed with a One-Step TUNEL Apoptosis Assay Kit (Beyotime, C1086, Shanghai, China) according to the manufacturer's protocol. Images were acquired with an Olympus FSX100 microscope (Olympus, Tokyo, Japan).

Lipidomics analysis

Lipidomics analysis was performed by LipidALL Technologies Co., Ltd. (Changzhou, China). Lipids were extracted from approximately 20 mg tissues or 1×10^6 cells using the method described previously[18].

Mass spectrometry

Liquid chromatography (LC) with tandem mass spectrometry (MS) was carried out by BGI Tech Solutions Co., Ltd (BGI Shenzhen, Guangdong, China). Protein pellets were digested with trypsin to a protein ratio of 1:20 and incubated at 37°C for 4 h. For each sample, the equivalent of 2–5 mg of protein was loaded into the LC-MS

/MS.

Xenograft mouse model

The six-week-old male nude mice used in this study were purchased from Nanjing Medical University Animal Center. For intracranial GBM xenograft experiments, PG7 cells lentivirally transduced with firefly luciferase (Fluc) were implanted into the frontal subdural region. The IVIS Imaging System (Caliper Life Sciences) was used to measure intracranial tumor growth. Each mouse was intraperitoneally injected with 10 mg D-luciferin (YEASEN, Shanghai, China) before imaging. The Living Images software package (Caliper Life Sciences) was used to analyze the integrated flux of photons in each region. The procedures were approved by the Animal Management Rule of the Chinese Ministry of Health (documentation 55, 2001) and the Nanjing Medical University Animal Experimental Ethics Committee (Ethics number: IACUC-1907006).

Statistical analyses

Statistical analyses were performed using the Prism 8.0.2 software (GraphPad Software, USA). Quantitative data were compared using a Student's *t*-test between two samples or one-way analysis of variance (ANOVA) for multiple samples. Statistical significance in Kaplan–Meier survival curves were calculated with the log-rank test. Data of subcutaneous tumor diameters in each group were analyzed using a two-way ANOVA. All results were indicated as the mean \pm S.D. and repeated in at least three independent experiments. P value < 0.05 was considered as the significant difference.

Results

Acsl4 contributed to lipidomic differences in gliomas

To investigate the underlying roles of ferroptosis in gliomas, microarray assays were firstly performed to identify lipid oxidation events by analyzing all major PE species in low-grade glioma (LGG) and glioblastoma (GBM) specimens. We found that AA- and AdA-containing PE (18:0/20:4 and 18:0/22:4, respectively) species were strikingly reduced in GBM *versus* LGG tissues (Fig. 1A) and cells (Fig. 1B). Then, we compared levels of oxidized lipids formed in erastin treated LGG and GBM cells. Similar to the results above, GBM cells suppressed the formation of doubly and triply oxidized AA- and AdA-containing PE species treated with erastin, in contrast with LGG cells (Fig. 1C). Because 12-HETE and 15-HETE are known as products of lipid peroxidation and are increasingly recognized as markers of ferroptosis, we found that the levels of both acids were decreased in GBM *versus* LGG specimens (Fig. 1D).

Previously published studies have revealed that some encoding proteins played crucial roles in lipid biosynthesis, especially in catalyzing PE-AA and PE-AdA, which represented preferred substrates for oxidation[15]. Next, we detected endogenous levels of four proteins— Acsl4, GPX4, LPCAT3 and 15-LOX in LGG and GBM specimens using western blot (WB). Acsl4 was selected for further analysis because other proteins showed no difference in expression between LGGs and GBMs (Fig. 1E, Supplementary. Fig. 1A). Immunohistochemical (IHC) staining also confirmed that GBMs showed markedly decreased Acsl4 protein expression compared with LGGs (Fig. 1F). Then, analysis of Acsl4 expression in public databases such as The Cancer Gene Atlas (TCGA) and Rembrandt revealed its relatively low expression in GBM compared with LGG (Fig. 1G). Kaplan–Meier analysis also demonstrated that patients with low Acsl4 expression levels displayed reduced overall survival time, while gliomas high in Acsl4 expression favored prolonged survival (Fig. 1H). Patient-derived glioma cells PL1 and PG7 were respectively isolated from discarded LGG1 and GBM7 specimens using WB (Supplementary. Fig. 1B). Additionally, we found that various glioma cell lines such as U87, U251, T98, PL1, and PG7 showed downregulated Acsl4 protein expression, in contrast with normal human astrocytes (NHAs) in culture (Supplementary. Fig. 1C). Therefore, we selected PL1 and PG7 cells for subsequent experiments. Our general supposition was that GBM might escape ferroptosis via genetic deficiency of Acsl4, which plays an important role in glioma lipidomics and serves as a vital ferroptosis marker in glioma.

Acsl4 participated in mitochondrial-morphology regulation in ferroptosis

Kagan *et al.* has elaborated that genetic and pharmacological suppression of Acsl4 markedly increases the resistance of mitochondria to RSL3-induced outer-membrane rupture, possibly constituting an anti-ferroptotic rescue pathway[16]. Given the mitochondrion is a main organelle for cellular oxidative phosphorylation and ROS production[19], we wished to unambiguously determine whether mitochondria were affected in Acsl4-dependent ferroptosis in glioma cells. Ferroptosis is known to differ from other forms of cell death that do not involve mitochondrial damage in cancer cells, but it contains significant morphological changes in mitochondria such as mitochondrial fragmentation and enlargement of cristae[5]. We observed that compared with GBM cells, the mitochondrial morphology of LGG cells was

liable to show more fragmentation accumulation around the nucleus in a dose-dependent manner in response to erastin toxicity (Fig. 2A). Quantification of mitochondrial length changed significantly at 1 μ M in PL1 cells but showed no difference until 5 μ M in PG7 cells (Fig. 2B). Furthermore, transmission electronic microscopy (TEM) revealed that PL1 cells treated with 1 μ M erastin and PG7 cells treated with 5 μ M erastin for 6 h had shrunken mitochondria and collapsed outer membranes with decreased microvilli, compared with cells that had been treated with the previous concentration (Fig. 2C). Therefore, we speculated that GBM cells tended to maintain a network of tubules, this morphology being characteristic of healthy and functional mitochondria, potentially due to low expression of Acsl4.

To investigate this possibility, we depleted PL1 cells Acsl4 of via short-hairpin ribonucleic acid (shRNA) knockdown, creating shAcsl4 cells, and stably transfected these into PG7 cells, creating Lv-Acsl4 cells. Protein and genetic levels of Acsl4 were detected via WB and quantitative reverse-transcription polymerase chain reaction (qRT-PCR; Fig. 2D and E). Since accumulation of lipid ROS is an end product of lipid peroxidation and a hallmark of ferroptosis in glioma, we estimated levels of lipid peroxidation using C11 BODIPY 581/591, a dye that is sensitive to lipid peroxidation. We found that after erastin treatment, ROS accumulation decreased to approximately one third in PL1 cells but roughly tripled in PG7 cells compared with control (Fig. 2F). We verified this finding using another independent probe, MDA (Fig. 2G). Moreover, both 12-HETE and 15-HETE levels were reduced when Acsl4 was knocked down in PL1 cells and increased when Acsl4 was overexpressed in PG7 cells (Fig. 2H and I). Additionally, as important antioxidants, reduced form GSH and GPX activity were upregulated in PL1–shAcsl4 cells, indicating that ferroptosis was suppressed in these cells, whereas they were downregulated in PG7–Lv-Acsl4 cells, indicating that ferroptosis was promoted therein (Fig. 2J and K). Furthermore, consistent with a prior study confirming subcellular localization of a lipid ROS probe via confocal-fluorescence microscopy (CFM), we found that in both PL1 and PG7 cells treated with erastin, the oxidized probe appeared in a distribution significantly colocalized with mitochondria and with the plasma membrane, with relatively high expression of Acsl4 (Fig. 2L). More importantly, the mitochondrial network of PL1–shAcsl4 cells was more elongated than that of PL1–shctrl cells, while PG7–Lv-Acsl4 cells became more fragmented and less elongated than PG7–vector cells. Therefore, we concluded that the mitochondrion was a primary site of Acsl4-dependent ferroptosis in glioma cells and that mitochondrial morphology could be affected by expression of Acsl4 in glioma ferroptosis.

Drp1 phosphorylation was essential for Acsl4-dependent ferroptosis

To establish potential regulators of Acsl4, we identified the proteins pulled down. Compared with control, we distinctly observed enrichment of proteins and a prominent band resolved at approximately 83 kDa, as shown in the sodium dodecyl sulfate polyacrylamide gel electrophoresis (SDS-PAGE) images in Figure 3A. Simultaneously, we analyzed whole-eluted samples without bias via mass spectrometry (MS). Next, we detected Drp1 as the most enriched protein. As expected, Drp1 was immunoprecipitated by sepharose-A coated with Acsl4 antibodies but not by immunoglobulin G (IgG; Fig. 3B), which was also confirmed by CFM (Fig. 3C).

Drp1 is well known for its role in regulating mitochondrial morphology[20], which was recently confirmed to be related to erastin-induced ferroptosis in melanoma cells[21]. Additionally, Drp1 deficiency leads to mitochondrial elongation and mitochondrial tubules connection, similar to the morphology of mitochondria that are insensitive to ferroptosis [22]. Therefore, we detected expression patterns of Drp1 in LGG and GBM samples using WB. Interestingly, we found no difference in expression of Drp1 protein between LGGs and GBMs (Supplementary. Fig. 2A and B). As is well known, Drp1 activity in glioma cells is regulated by post-translational modifications, mainly by phosphorylation: while serine 616 (Ser616) residue is an activation site, Ser637 residue is a repression site [23, 24]. We next determined levels of phosphorylated Drp1 (p-Drp1) at Ser616 and Ser637 in primary LGG and GBM clinical specimens using Western blot and IHC. In every model we tested, p-Drp1 (Ser637) levels were significantly increased in GBMs compared with LGGs, while p-Drp1 (Ser616) and Drp1 levels did not differ between the two specimen types, suggesting that GBM cells had attenuated activity of Drp1. Moreover, both LGG and GBM specimens showed decreased Drp1 Ser637 expression when treated with erastin (Fig. 3D–G), indicating that inactivation of Drp1 by phosphorylation at Ser637 was suppressed in erastin-induced ferroptosis. Then, to determine whether Drp1 phosphorylation was relevant to Acsl4-dependent ferroptosis, we generated a gain-of-function Drp1 containing both S637E (to mimic inhibitory phosphorylation) mutations in PL1 cells and S637A (to block inhibitory phosphorylation–dephosphorylation) mutations in PG7 cells (Supplementary. Fig. 2C and D). We found that after erastin treatment, both lipid ROS and MDA levels were significantly decreased in PL1 cells transduced by lentivirus expressing mutated Drp1^{S637E} compared with control vector, synchronous with 12-HETE and 15-HETE levels (Fig. 3I and J, Supplementary. Fig. 3A and B). Moreover, reduced-form GSH and GPX activities were enhanced by the inactivation of Drp1 (Supplementary. Fig. 3C and D). CFM revealed that the morphology of mitochondria in PL1–Drp1^{S637E} cells became more filamentous. However, when we overexpressed Acsl4 in PL1–Drp1^{S637E} cells, the aforementioned changes in lipid mediators and mitochondrial morphology were reversed by Acsl4 restoration (Fig. 3H–J), suggesting that phosphorylation of Drp1 at Ser637 in LGG cells strongly inhibited Acsl4-dependent ferroptosis. Correspondingly, lipid ROS and MDA levels were markedly increased in PG7 cells transduced by lentivirus expressing mutated Drp1^{S637A} compared with control vector cells (Fig. 3H–J), synchronous with 12-HETE and 15-HETE levels (Supplementary. Fig. 3A and B). In addition, reduced-form GSH and GPX activities were exhausted by activation of Drp1 (Supplementary. Fig. 3C and D). Moreover, PG7–Drp1^{S637A} cells tended to show a fragmented mitochondrial phenotype. However, when we knocked down Acsl4 in PG7–Drp1^{S637A} cells, those surrogate markers were once again reversed (Fig. 3H–J, Supplementary. Fig. 3A–D), suggesting that dephosphorylation of Drp1 at Ser637 in GBM cells strongly induced Acsl4-dependent ferroptosis. Taken together, these results demonstrated that dephosphorylation of Drp1 at Ser637 inhibited mitochondrial filamentation, which was essential for inducing Acsl4-dependent ferroptosis in glioma cells.

Hsp90 regulated Drp1 phosphorylation via calcineurin in gliomas

Through MS, we found that Hsp90 as well as Drp1 interacted with Acsl4 (Fig. 4A). Hsp90, as a global regulator of tumor cell metabolism in mitochondria including oxidative phosphorylation and redox networks, is defined as a common regulatory node in both necroptosis and ferroptosis[25, 26]. Co-immunoprecipitation (co-IP) experiments in PL1 and PG7 cells showed that Acsl4, Drp1, and Hsp90 interacted with each other (Fig. 4B), and confocal images showed that Hsp90 colocalized with Acsl4 and Drp1 in the mitochondrial outer membrane (Fig. 4C).

A previous study revealed calcineurin (CN) to dephosphorylate Drp1 at Ser637 in many types of cells[27]; Hsp90 has been reported to bind to CN and stimulates its activity[28]. Therefore, we next verified the effects of Hsp90 on CN and Drp1 in PL1 cells and in PG7 cells in the context of glioma, particularly the effects of Hsp90 level on the Drp1–Acsl4 axis in erastin-induced ferroptosis using WB. As expected, we found that knockdown of Hsp90 in PL1 cells promoted Drp1 (Ser637) phosphorylation while downregulating CN and Acsl4 expression. Of note, the expression level of Drp1 remained constant. Similarly, when we overexpressed Hsp90 in PG7 cells, we also found that the Drp1–Acsl4 axis was activated (Fig. 4D).

Promotion of the Hsp90–Acsl4 pathway enhanced erastin sensitivity *in vitro*

We sought to determine the relevance of the Hsp90–Acsl4 pathway in erastin-induced ferroptosis *in vitro*. First, we investigated the effect of Hsp90 on Drp1 and Acsl4 protein levels in erastin-induced ferroptosis. As shown in Figure 5A, shHsp90 significantly promoted Drp1^{Ser637} level and inhibited CN and Acsl4 expression; meanwhile, Drp1 expression remained unchanged in PL1 cells. Similarly, in PG7 cells, Lv-Hsp90 markedly inhibited Drp1 (Ser637) phosphorylation and promoted CN and Acsl4 expression, while Drp1 expression remained unchanged.

Next, we examined whether Hsp90 could sensitize glioma cells to Acsl4-dependent ferroptosis. As shown in Figure 5C and D, Hsp90 significantly ameliorated lipid ROS and MDA generation in PL1 and PG7 cells. The Hsp90–Acsl4 pathway also affected 12-HETE and 15-HETE levels (Fig. 5E and F). Moreover, GSH was exhausted by the promotion of Hsp90, with GPX activity downregulated in glioma cells (Fig. 5G and H). Furthermore, CFM revealed that mitochondria extended throughout the cell body to sites distal from the nucleus when the Hsp90–Acsl4 pathway was downregulated, and they showed more fragmentation accumulation around the nucleus when this pathway was upregulated (Fig. 5B).

We further investigated the mechanisms of the Hsp90–Acsl4 pathway on ferroptosis by studying the cytotoxic efficacy of erastin in glioma cells. Colony formation, EdU, and TUNEL experiments were performed to evaluate cell proliferation. These results showed that in all highly Acsl4-expressing cells (Lv-Hsp90, Drp1^{S637A}, and Lv-Acsl4), the ability of erastin to inhibit cell proliferation was notably enhanced; meanwhile, in cells with reduced Acsl4 expression levels (shHsp90, Drp1^{S637E}, and shAcsl4), this ability was comparably reduced (Fig. 6A–C). We also performed CCK-8 and cytotoxicity (LDH) assays to confirm

that the Hsp90–Acsl4 pathway had a significant effect on cell proliferation in erastin-induced ferroptosis (Supplementary. Fig. 4A and B). Of note, apoptosis was not affected in PL1 and PG7 cells with changed Acsl4 levels, as indicated by the comparable activity and expression levels of cleaved Caspase-3 (Supplementary. Fig. 4C). Therefore, these results confirmed that Hsp90–Acsl4 pathway upregulation promoted ferroptosis and decreased proliferation of glioma cells. Conversely, downregulation of this pathway decreased ferroptosis and promoted proliferation of glioma cells.

Promotion of the Hsp90–Acsl4 pathway enhanced erastin sensitivity *in vivo*

To examine whether promotion of the Hsp90–Acsl4 pathway also increased tumor sensitivity to erastin *in vivo*, we first established mouse subcutaneous and orthotopic models via PG7 cells to confirm the sensitivity of parental GBM cells to different concentrations of erastin. Five days after PG7 implantation, mice were treated intraperitoneally (i.p.) with erastin at different concentrations (5, 10, 15, or 20 mg/kg⁻¹/day⁻¹ per mouse) or dimethyl sulfoxide (DMSO; 0.3%) every 2 days (Fig. 7A). Subcutaneous tumors transplanted with PG7 cells were visible at about 10 days and we found that erastin's ability to slow tumor growth rate changed significantly between 10 and 15 mg (Fig. 7B). At day 35 after transplantation, tumors were collected and weighed (Fig. 7C and D), confirming previous results. At the same time, we traced tumor progression using *in vivo* bioluminescence imaging every 7 days; the images revealed that the antitumor effect of erastin did not make a difference until 15 mg (Fig. 7F). Similarly, mouse survival rate also exhibited an obvious difference between erastin 10 mg and erastin 15 mg (Fig. 7E).

Next, we assessed the therapeutic value of Acsl4 overexpression on GBM cells *in vivo*. Five days after PG7 implantation, mice were treated i.p. with erastin (10 mg/kg⁻¹/day⁻¹ per mouse) or DMSO (0.3%) every 2 days (Fig. 8A). We found that when erastin was combined with Hsp90 or Acsl4 overexpression, tumor inhibition was more significant. Drp1^{S637E} inhibited the growth of erastin-treated Lv-Hsp90 PG7 cells to the same degree that it did to erastin-treated PG7 tumors (Fig. 8B–D). Moreover, bioluminescent imaging revealed that overexpression of Acsl4 effectively increased the sensitivity of GBM xenografts to erastin treatment. Mice receiving combined treatment showed considerably smaller tumor volume than other mice (Fig. 8G) and had dramatically prolonged lifespans (Fig. 8E). Orthotopic glioblastoma development markedly decreased mouse weight, which was mitigated by erastin administration (Fig. 8F).

We next assessed levels of primary Hsp90–Acsl4 pathway proteins in mouse tumors using IHC. Consistent with the *in vitro* results, Hsp90 overexpression mitigated p-Drp1^{Ser637} levels and enhanced Acsl4 expression, whereas Drp1 level did not change significantly (Fig. 9A). Additionally, mice with Hsp90–Acsl4 overexpression showed decreased levels of Ki-67 (Fig. 9B). TUNEL assays demonstrated that erastin mildly promoted cell death *in vivo*. Hsp90 and Acsl4 overexpression intensified erastin-induced PG7 cell death, but Drp1^{S637E} limited this effect (Fig. 9C). Because mitochondria play a pivotal role in Acsl4-dependent ferroptosis, we assessed mitochondrial morphology in transplanted GBM tumors

via TEM. Shrunken mitochondria and ruptured outer mitochondrial-membrane, possibly related to the typical mitochondrial changes caused by ferroptosis were found in the erastin, erastin + Lv-Hsp90, and erastin + Lv-Hsp90+ Drp1^{S637E} +Lv-Acsl4 groups. These changes were alleviated in the erastin + Lv-Hsp90 +Drp1^{S637E} group (Fig. 10A). Finally, we performed microarray assays to identify lipid oxidation events by analyzing all major PE species in mouse tumor specimens. We found that AA- and AdA-containing PE (18:0/20:4 and 18:0/22:4, respectively) species were strikingly increased in the erastin groups, especially the erastin + Lv-Hsp90 and the erastin + Lv-Hsp90 + Drp1^{S637E} + Lv-Acsl4 group (Fig. 10B). Overall, these data demonstrated that Acsl4 could serve as a potential therapeutic target to enhance the benefits of erastin.

Discussion

Herein, we described a underlying mechanism for the regulation of ferroptosis between different grades of gliomas: LGGs could have a considerable effect on the decision-making because ferroptosis was more likely to happen in LGGs due to the high Acsl4 expression levels of LGGs. Studies show that curing glioma with existing treatments is difficult, but it is obvious that with appropriate management, patients with LGG have better prognosis and survival than those with GBM[1]. Previous studies have shown that ferroptosis suppression contributed to the progression and poor prognosis of glioma[29–31]. Consistent with the prior studies, we observed reduced viability and inhibited proliferation of glioma cells in erastin-induced ferroptosis. Considering that the complex central nervous system is under frequent oxidative stress[32], this mechanism might represent the role of ferroptosis in the prognosis and treatment of gliomas.

Stockwell *et al.* elucidated that ferroptosis is a form of RCD that occurs as a consequence of lethal-lipid peroxidation[33]. Furthermore, Xie Y pointed out that changes in the morphology of mitochondria, as representative RCD-executing organelles, are important features that distinguish ferroptosis from other forms of programmed death[4]. In this study, differences in lipidomics and mitochondrial morphology suggested that LGGs were more sensitive to ferroptosis. Database analyses demonstrated that Acsl4 was genetically expressed at relatively high levels in LGGs *versus* GBMs, which was confirmed by protein levels. Kagan has revealed that Acsl4 is dedicated to shaping the lipidomic of cells by playing an important role in determining sensitivity *versus* resistance to ferroptosis[16]. Therefore, we hypothesized that the reduction of ferroptosis in GBMs might be attributable to a reduction in Acsl4 expression. To validate the role of Acsl4 in glioma ferroptosis, we respectively transfected shAcsl4 and Acsl4 overexpression plasmids into two different primary glioma cell lines, PL1 and PG7 cells. Lipid ROS, MDA, 12-HETE, 15-HETE, and GSH and GPX activities, which are main products of cellular oxidative metabolism, are regarded as Acsl4-dependent ferroptosis indicators. The results demonstrated that Acsl4 could be the factor that makes a difference in ferroptotic sensitivity between different grades of gliomas.

Subsequently, we found Drp1 and Hsp90 to interact with Acsl4 via immunoprecipitation. However, there were no differences in the Drp1 expression levels between LGGs and GBMs, which led to a standstill with the study. Apart from gene expression, protein modifications—including phosphorylation, ubiquitination,

methylation, SUMOylation, and acetylation—provide valuable routes for further exploration in cancer research[34]. We found that Drp1 (Ser637) phosphorylation inhibited Drp1 activity in glioma cells and suppressed Acsl4-dependent ferroptosis by diminishing lipid ROS production and inducing mitochondria to exhibit an interconnected phenotype. Accordingly, these findings suggest that similar to other RCDs such as autophagy and apoptosis that occur in mitochondria, ferroptosis in mitochondria was closely associated with the induction of Drp1 phosphorylation. Of note, Drp1 phosphorylation is known to be involved in mitochondrial fission and fusion[35, 36]. In this study, Drp1 dephosphorylation at Ser637, inducing a mitochondrial-morphology shift in Acsl4-dependent ferroptosis, was highly similar to Drp1-mediated mitochondrial fission, indicating that mitochondrial-morphology shift could be closely related to mitochondrial fission. Nonetheless, the molecular mechanisms by which oncogenic signaling pathways could alter mitochondrial dynamics in glioma ferroptosis deserve further investigation.

HSPs mainly protect cells against harmful stimuli by stabilizing unfolded or misfolded peptides and by repairing or promoting the degradation of denatured proteins[25]; these activities of HSPs are reported to render cancer cells resistant to certain RCDs such as apoptosis and necrosis[37]. Previously published studies have mostly emphasized Hsp90, an important member of the HSP family, as a target to overcome chemotherapy resistance mechanisms and improve sensitivity to temozolomide (TMZ) in gliomas[38, 39]. Although Hsp90 is rarely reported in ferroptosis, certain other HSPs such as HSPB1 and HSPA5 have been demonstrated to downregulate erastin-induced ferroptosis, mediating ferroptosis resistance. However, we found that Hsp90 positively promoted erastin-induced ferroptosis. Mechanistically, phosphorylated HSPB1 downregulates ferroptosis by reducing cellular iron uptake and lipid ROS production[40], while increased HSPA5 expression suppresses ferroptosis via direct inhibition of GPX4 protein degradation[41]. Our findings suggested that Hsp90-dependent Drp1 dephosphorylation and Acsl4 expression could sensitize glioma cells to erastin-induced ferroptosis *in vitro* and *in vivo*, because the Hsp90–Acsl4 pathway significantly enhanced the production of lipid peroxidation and increased mitochondrial fragmentation. Hsp90 therefore served as a positive rather than a negative regulator of ferroptosis due to molecular-pathway differences.

Of late, researchers in cancer therapy have been paying more and more attention to utilizing ferroptosis. Consequently, several clinical drugs are drawing increasing appreciation because of their capacity for inducing ferroptosis in cancer cells. Erastin is the prototype ferroptosis inducer that can reduce GSH levels by inhibiting system Xc- directly[42]. Sulfasalazine (SAS), an anti-inflammatory drug, can induce ferroptosis in a series of cancer cell lines (HT-1080, BJeLR, Calu-1, 143B) and has been used in combination therapy to enhance the therapeutic efficacy of other chemotherapeutics against glioma[43, 44]. Dihydroartemisinin (DHA) induces ferroptosis in head-and-neck carcinoma cells by increasing overall and mitochondrial ROS levels[45]. Sorafenib, a clinically approved multi-kinase inhibitor for the treatment of advanced carcinoma, induces ferroptosis independently[43]. Other small-molecule inducers of ferroptosis include FIN56, which degrades GPX4, binds to squalene synthase (SQS), and depletes the antioxidant coenzyme Q₁₀ (CoQ10)[46]; statins, which inhibit 3-hydroxy-3-methylglutaryl-CoA reductase (HMGCR), decrease GPX4 levels, and block biosynthesis of CoQ10[47]; and BAY

87–2243, which inhibits mitochondrial complex I (MC-I)[21]. Most importantly, erastin and its derivatives have successfully treated diffuse large B-cell lymphoma (DLBCL) in a SUDHL6 cell xenograft animal model[48].

Notably, the dose of erastin (10 mg/kg, i.p., twice every other day) we explored and used in treating glioma was lower than that we used in meningioma treatment before, which was 15 mg/kg, i.p., twice every other day[49]. Moreover, compared with the data published before, we found that Sun X used 20 mg/kg intravenously (i.v.), twice daily every other day in treating HeLa-derived subcutaneous tumors [40], and that Hao S used 20 mg/kg, i.p., twice every other day in treating gastric cancer [50]. The low-dose treatment not only had no adverse events, but also had remarkable anti-tumor effects, which adequately proved that the induction of ferroptosis is practical and feasible in viable anti-glioma tactics. Furthermore, promotion of Acsl4 contributed to efficient tumor inhibition and obvious survival improvement, due to the increasing sensitivity of glioma to erastin-induced ferroptosis.

Conclusions

In summary, activation of the Hsp90–Drp1–Acsl4 pathway upregulated erastin-induced ferroptosis. Furthermore, CN-mediated Drp1 dephosphorylation was required for Acsl4-dependent ferroptosis, possibly through regulating lipid ROS production and altering mitochondrial morphology. In particular, genetic promotion of the Hsp90–Acsl4 pathway significantly improved the anticancer activity of erastin *in vitro* and *in vivo*. Our study not only uncovered an important role of Acsl4 in predicting patient prognosis but also suggested an underlying regulatory mechanism of Acsl4 as a potential therapeutic target to enhance the effect of ferroptosis-inducing therapy for glioma.

Abbreviations

ROS: Reactive oxygen species; Acsl4: Acyl–coenzyme A (CoA) synthetase long-chain family member 4; Hsp90: Heat shock protein 90; Drp1: dynamin-related protein 1; GPX4: glutathione peroxidase 4; PUFAs: polyunsaturated fatty acids; PE: phosphatidylethanolamine; AA/AdA: arachidonic/ adrenic acid; 12/15-HETE: 12/15-hydroxyeicosatetraenoic acids; MDA: Malondialdehyde

Declarations

Author contributions

J.J. and N.L. designed and interpreted experiments. Z.M., W.T., Z.Y.B., S.M.L., G.C.S. and L.X. performed experiments. H.L.C., Y.F.Y., Y.M.T., L.C. analysed the data. Z.M. and J.J. wrote the manuscript. All authors critically read the manuscript.

Acknowledgements

We thank the other members of our laboratory.

Author details

¹ Department of Neurosurgery, the First Affiliated Hospital of Nanjing Medical University, Nanjing, China.

² LipidALL Technologies Company Limited, Changzhou, China.

Competing interests

The authors declare no competing interests.

Availability of data and materials

The datasets used and/or analyzed during the current study are available from the corresponding author on reasonable request.

Consent for publication

All authors agreed on the manuscript.

Ethics approval and consent to participate

The studies were reviewed and approved by the Ethics Committee of the First Affiliated Hospital of Nanjing Medical University and the Nanjing Medical University Animal Experimental Ethics Committee.

Funding

This study was funded by the National Natural Science Foundation of China (Grant No. 81972153), Jiangsu Province's Key Discipline of Medicine (Grant No. XK201117), Jiangsu Province Innovative Team (Grant No. NR17).

References

1. Tan AC, Ashley DM, Lopez GY, Malinzak M, Friedman HS, Khasraw M. Management of glioblastoma: State of the art and future directions. *CA Cancer J Clin.* 2020;70(4): 299–312. DOI:10.3322/caac.21613.

2. Mariappan A, Goranci-Buzhala G, Ricci-Vitiani L, Pallini R, Gopalakrishnan J. Trends and challenges in modeling glioma using 3D human brain organoids. *Cell Death Differ.* 2021;28(1): 15–23.DOI:10.1038/s41418-020-00679-7.
3. Dixon SJ, Lemberg KM, Lamprecht MR, Skouta R, Zaitsev EM, Gleason CE, *et al.* Ferroptosis: an iron-dependent form of nonapoptotic cell death. *Cell.* 2012;149(5): 1060–1072.DOI:10.1016/j.cell.2012.03.042.
4. Xie Y, Hou W, Song X, Yu Y, Huang J, Sun X, *et al.* Ferroptosis: process and function. *Cell Death Differ.* 2016;23(3): 369–379.DOI:10.1038/cdd.2015.158.
5. Neitemeier S, Jelinek A, Laino V, Hoffmann L, Eisenbach I, Eying R, *et al.* BID links ferroptosis to mitochondrial cell death pathways. *Redox Biol.* 2017;12:558–570.DOI:10.1016/j.redox.2017.03.007.
6. Kagan VE, Mao G, Qu F, Angeli JP, Doll S, Croix CS, *et al.* Oxidized arachidonic and adrenic PEs navigate cells to ferroptosis. *Nat Chem Biol.* 2017;13(1): 81–90.DOI:10.1038/nchembio.2238.
7. Yang WS, Kim KJ, Gaschler MM, Patel M, Shchepinov MS, Stockwell BR. Peroxidation of polyunsaturated fatty acids by lipoxygenases drives ferroptosis. *Proc Natl Acad Sci U S A.* 2016;113(34): E4966-4975.DOI:10.1073/pnas.1603244113.
8. Friedmann Angeli JP, Schneider M, Proneth B, Tyurina YY, Tyurin VA, Hammond VJ, *et al.* Inactivation of the ferroptosis regulator Gpx4 triggers acute renal failure in mice. *Nat Cell Biol.* 2014;16(12): 1180–1191.DOI:10.1038/ncb3064.
9. Li Y, Feng D, Wang Z, Zhao Y, Sun R, Tian D, *et al.* Ischemia-induced ACSL4 activation contributes to ferroptosis-mediated tissue injury in intestinal ischemia/reperfusion. *Cell Death Differ.* 2019;26(11): 2284–2299.DOI:10.1038/s41418-019-0299-4.
10. Yang WS, SriRamaratnam R, Welsch ME, Shimada K, Skouta R, Viswanathan VS, *et al.* Regulation of ferroptotic cancer cell death by GPX4. *Cell.* 2014;156(1-2): 317–331.DOI:10.1016/j.cell.2013.12.010.
11. Tsoi J, Robert L, Paraiso K, Galvan C, Sheu KM, Lay J, *et al.* Multi-stage Differentiation Defines Melanoma Subtypes with Differential Vulnerability to Drug-Induced Iron-Dependent Oxidative Stress. *Cancer Cell.* 2018;33(5): 890–904 e895.DOI:10.1016/j.ccell.2018.03.017.
12. Zhao Y, Li Y, Zhang R, Wang F, Wang T, Jiao Y. The Role of Erastin in Ferroptosis and Its Prospects in Cancer Therapy. *Onco Targets Ther.* 2020;13:5429–5441.DOI:10.2147/OTT.S254995.
13. Killion EA, Reeves AR, El Azzouny MA, Yan QW, Surujon D, Griffin JD, *et al.* A role for long-chain acyl-CoA synthetase-4 (ACSL4) in diet-induced phospholipid remodeling and obesity-associated adipocyte dysfunction. *Mol Metab.* 2018;9:43–56.DOI:10.1016/j.molmet.2018.01.012.
14. Yang WS, Stockwell BR. Ferroptosis: Death by Lipid Peroxidation. *Trends Cell Biol.* 2016;26(3): 165–176.DOI:10.1016/j.tcb.2015.10.014.
15. D'Herde K, Krysko DV. Ferroptosis: Oxidized PEs trigger death. *Nat Chem Biol.* 2017;13(1): 4–5.DOI:10.1038/nchembio.2261.
16. Doll S, Proneth B, Tyurina YY, Panzilius E, Kobayashi S, Ingold I, *et al.* ACSL4 dictates ferroptosis sensitivity by shaping cellular lipid composition. *Nat Chem Biol.* 2017;13(1): 91–98.DOI:10.1038/nchembio.2239.

17. Yuan H, Li X, Zhang X, Kang R, Tang D. Identification of ACSL4 as a biomarker and contributor of ferroptosis. *Biochem Biophys Res Commun*. 2016;478(3): 1338–1343.DOI:10.1016/j.bbrc.2016.08.124.
18. Lam SM, Zhang C, Wang Z, Ni Z, Zhang S, Yang S, *et al*. A multi-omics investigation of the composition and function of extracellular vesicles along the temporal trajectory of COVID-19. *Nat Metab*. 2021;3(7): 909–922.DOI:10.1038/s42255-021-00425-4.
19. Gao M, Yi J, Zhu J, Minikes AM, Monian P, Thompson CB, *et al*. Role of Mitochondria in Ferroptosis. *Mol Cell*. 2019;73(2): 354–363 e353.DOI:10.1016/j.molcel.2018.10.042.
20. Kraus F, Roy K, Pucadyil TJ, Ryan MT. Function and regulation of the divisome for mitochondrial fission. *Nature*. 2021;590(7844): 57–66.DOI:10.1038/s41586-021-03214-x.
21. Basit F, van Oppen LM, Schockel L, Bossenbroek HM, van Emst-de Vries SE, Hermeling JC, *et al*. Mitochondrial complex I inhibition triggers a mitophagy-dependent ROS increase leading to necroptosis and ferroptosis in melanoma cells. *Cell Death Dis*. 2017;8(3): e2716.DOI:10.1038/cddis.2017.133.
22. Ren X, Chen L, Xie J, Zhang Z, Dong G, Liang J, *et al*. Resveratrol Ameliorates Mitochondrial Elongation via Drp1/Parkin/PINK1 Signaling in Senescent-Like Cardiomyocytes. *Oxid Med Cell Longev*. 2017;20174175353.DOI:10.1155/2017/4175353.
23. Eugenio-Pérez D B-HA, Martínez-Klimova E, Pedraza-Chaverri J. Drp1-mediated Mitochondrial Fission in Glioma Malignancy. *Yale J Biol Med*. 2019; 2019 Sep 20(92(3)): 423-433
24. Taguchi N, Ishihara N, Jofuku A, Oka T, Mihara K. Mitotic phosphorylation of dynamin-related GTPase Drp1 participates in mitochondrial fission. *J Biol Chem*. 2007;282(15): 11521–11529.DOI:10.1074/jbc.M607279200.
25. Chae YC, Angelin A, Lisanti S, Kossenkov AV, Speicher KD, Wang H, *et al*. Landscape of the mitochondrial Hsp90 metabolome in tumours. *Nat Commun*. 2013;42139.DOI:10.1038/ncomms3139.
26. Wu Z, Geng Y, Lu X, Shi Y, Wu G, Zhang M, *et al*. Chaperone-mediated autophagy is involved in the execution of ferroptosis. *Proc Natl Acad Sci U S A*. 2019;116(8): 2996–3005.DOI:10.1073/pnas.1819728116.
27. Park J, Choi H, Kim B, Chae U, Lee DG, Lee SR, *et al*. Peroxiredoxin 5 (Prx5) decreases LPS-induced microglial activation through regulation of Ca(2+)/calcineurin-Drp1-dependent mitochondrial fission. *Free Radic Biol Med*. 2016;99392-404.DOI:10.1016/j.freeradbiomed.2016.08.030.
28. Huang G, Cong Z, Wang X, Yuan Y, Xu R, Lu Z, *et al*. Targeting HSP90 attenuates angiotensin II-induced adventitial remodelling via suppression of mitochondrial fission. *Cardiovasc Res*. 2020;116(5): 1071–1084.DOI:10.1093/cvr/cvz194.
29. Chen D, Fan Z, Rauh M, Buchfelder M, Eyupoglu IY, Savaskan N. ATF4 promotes angiogenesis and neuronal cell death and confers ferroptosis in a xCT-dependent manner. *Oncogene*. 2017;36(40): 5593–5608.DOI:10.1038/onc.2017.146.

30. Cheng J, Fan YQ, Liu BH, Zhou H, Wang JM, Chen QX. ACSL4 suppresses glioma cells proliferation via activating ferroptosis. *Oncol Rep.* 2020;43(1): 147–158.DOI:10.3892/or.2019.7419.
31. Wang Z, Ding Y, Wang X, Lu S, Wang C, He C, *et al.* Pseudolaric acid B triggers ferroptosis in glioma cells via activation of Nox4 and inhibition of xCT. *Cancer Lett.* 2018;42821–33.DOI:10.1016/j.canlet.2018.04.021.
32. Gilbert MR, Liu Y, Neltner J, Pu H, Morris A, Sunkara M, *et al.* Autophagy and oxidative stress in gliomas with IDH1 mutations. *Acta Neuropathol.* 2014;127(2): 221–233.DOI:10.1007/s00401-013-1194-6.
33. Stockwell BR, Friedmann Angeli JP, Bayir H, Bush AI, Conrad M, Dixon SJ, *et al.* Ferroptosis: A Regulated Cell Death Nexus Linking Metabolism, Redox Biology, and Disease. *Cell.* 2017;171(2): 273–285.DOI:10.1016/j.cell.2017.09.021.
34. Schaefer T, Lengerke C. SOX2 protein biochemistry in stemness, reprogramming, and cancer: the PI3K/AKT/SOX2 axis and beyond. *Oncogene.* 2020;39(2): 278–292.DOI:10.1038/s41388-019-0997-x.
35. Xie Q, Wu Q, Horbinski CM, Flavahan WA, Yang K, Zhou W, *et al.* Mitochondrial control by DRP1 in brain tumor initiating cells. *Nat Neurosci.* 2015;18(4): 501–510.DOI:10.1038/nn.3960.
36. Kashatus JA, Nascimento A, Myers LJ, Sher A, Byrne FL, Hoehn KL, *et al.* Erk2 phosphorylation of Drp1 promotes mitochondrial fission and MAPK-driven tumor growth. *Mol Cell.* 2015;57(3): 537–551.DOI:10.1016/j.molcel.2015.01.002.
37. Takayama S, Reed JC, Homma S. Heat-shock proteins as regulators of apoptosis. *Oncogene.* 2003;22(56): 9041–9047.DOI:10.1038/sj.onc.1207114.
38. Sauvageot CM, Weatherbee JL, Kesari S, Winters SE, Barnes J, Dellagatta J, *et al.* Efficacy of the HSP90 inhibitor 17-AAG in human glioma cell lines and tumorigenic glioma stem cells. *Neuro Oncol.* 2009;11(2): 109–121.DOI:10.1215/15228517-2008-060.
39. Canella A, Welker AM, Yoo JY, Xu J, Abas FS, Kesanakurti D, *et al.* Efficacy of Onalespib, a Long-Acting Second-Generation HSP90 Inhibitor, as a Single Agent and in Combination with Temozolomide against Malignant Gliomas. *Clin Cancer Res.* 2017;23(20): 6215–6226.DOI:10.1158/1078-0432.CCR-16-3151.
40. Sun X, Ou Z, Xie M, Kang R, Fan Y, Niu X, *et al.* HSPB1 as a novel regulator of ferroptotic cancer cell death. *Oncogene.* 2015;34(45): 5617–5625.DOI:10.1038/onc.2015.32.
41. Zhu S, Zhang Q, Sun X, Zeh HJ, 3rd, Lotze MT, Kang R, *et al.* HSPA5 Regulates Ferroptotic Cell Death in Cancer Cells. *Cancer Res.* 2017;77(8): 2064–2077.DOI:10.1158/0008-5472.CAN-16-1979.
42. Liang C, Zhang X, Yang M, Dong X. Recent Progress in Ferroptosis Inducers for Cancer Therapy. *Adv Mater.* 2019;31(51): e1904197.DOI:10.1002/adma.201904197.
43. Dixon SJ, Patel DN, Welsch M, Skouta R, Lee ED, Hayano M, *et al.* Pharmacological inhibition of cystine-glutamate exchange induces endoplasmic reticulum stress and ferroptosis. *Elife.* 2014;3e02523.DOI:10.7554/eLife.02523.

44. Sehm T FZ, Ghoochani A, Rauh M, Engelhorn T, Minakaki G, Dörfler A, Klucken J, Buchfelder M, Eyüpoglu IY, Savaskan N. Sulfasalazine impacts on ferroptotic cell death and alleviates the tumor microenvironment and glioma-induced brain edema. *Oncotarget* 2016 Jun 14(7(24)): 36021–36033. DOI:10.18632/oncotarget.8651.
45. Lin R, Zhang Z, Chen L, Zhou Y, Zou P, Feng C, *et al.* Dihydroartemisinin (DHA) induces ferroptosis and causes cell cycle arrest in head and neck carcinoma cells. *Cancer Lett.* 2016;381(1): 165–175. DOI:10.1016/j.canlet.2016.07.033.
46. Shimada K, Skouta R, Kaplan A, Yang WS, Hayano M, Dixon SJ, *et al.* Global survey of cell death mechanisms reveals metabolic regulation of ferroptosis. *Nat Chem Biol.* 2016;12(7): 497–503. DOI:10.1038/nchembio.2079.
47. Viswanathan VS, Ryan MJ, Dhruv HD, Gill S, Eichhoff OM, Seashore-Ludlow B, *et al.* Dependency of a therapy-resistant state of cancer cells on a lipid peroxidase pathway. *Nature.* 2017;547(7664): 453–457. DOI:10.1038/nature23007.
48. Zhang Y, Tan H, Daniels JD, Zandkarimi F, Liu H, Brown LM, *et al.* Imidazole Ketone Erastin Induces Ferroptosis and Slows Tumor Growth in a Mouse Lymphoma Model. *Cell Chem Biol.* 2019;26(5): 623–633 e629. DOI:10.1016/j.chembiol.2019.01.008.
49. Bao Z, Hua L, Ye Y, Wang D, Li C, Xie Q, *et al.* MEF2C silencing downregulates NF2 and E-cadherin and enhances Erastin-induced ferroptosis in meningioma. *Neuro Oncol.* 2021. DOI:10.1093/neuonc/noab114.
50. Hao S, Yu J, He W, Huang Q, Zhao Y, Liang B, *et al.* Cysteine Dioxygenase 1 Mediates Erastin-Induced Ferroptosis in Human Gastric Cancer Cells. *Neoplasia.* 2017;19(12): 1022–1032. DOI:10.1016/j.neo.2017.10.005.

Figures

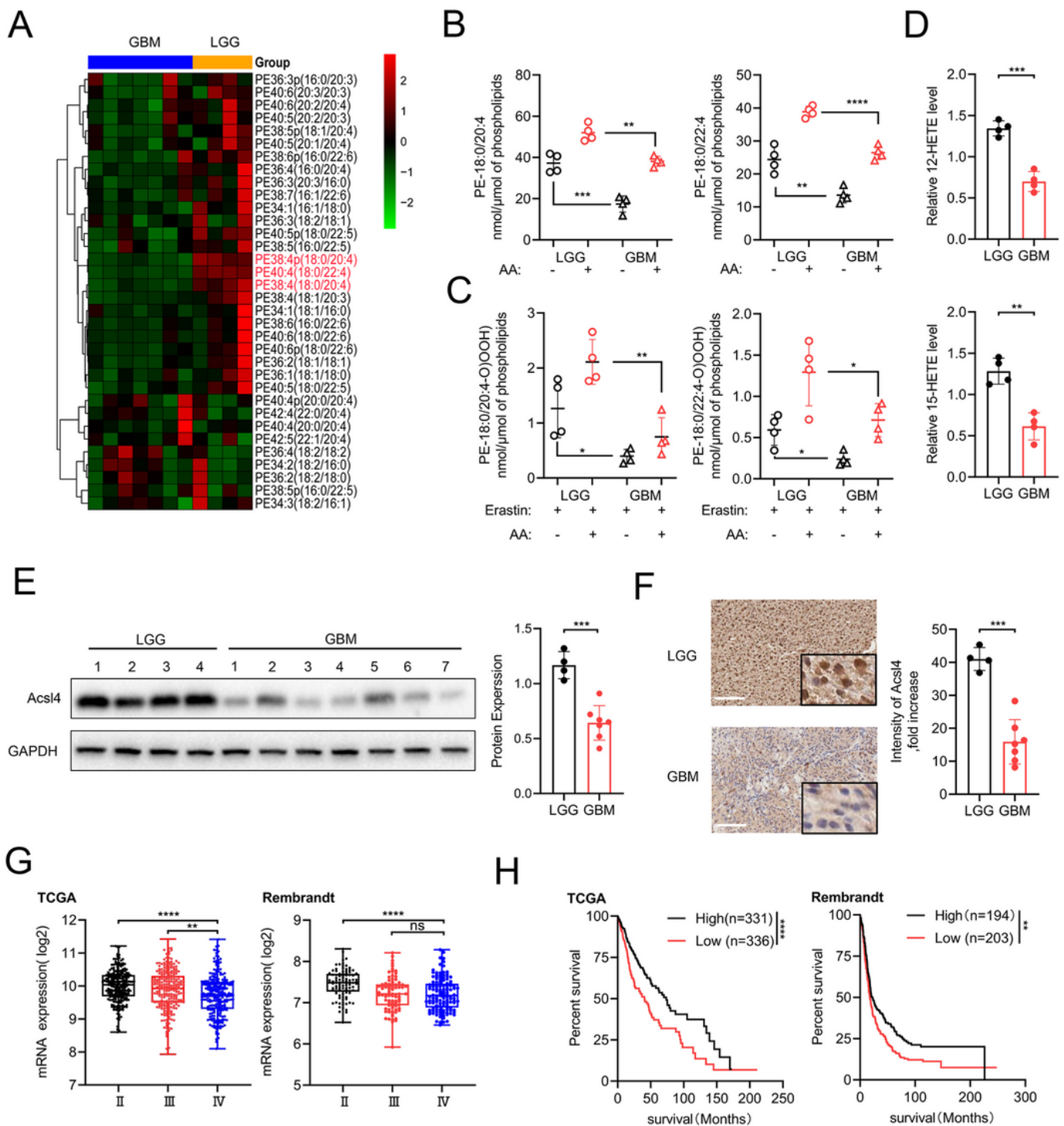


Figure 1

Acs14 contributed to lipidomics difference in gliomas.

(A) Heatmap of all major PE species were classified into LGG and GBM clusters. (B) Quantitative analysis of PE (18:0/20:4) and PE (18:0/22:4) in LGG and GBM cells in the absence or presence of AA. Cells were supplemented with AA (3.5 μ M, 16 h at 37°C). Data indicated as mean \pm S.D. (n = 4 experiments). (C)

Quantitative analysis of hydroperoxy-PE (18:0/20:4) and hydroperoxy-PE (18:0/22:4) in LGG and GBM cells in the absence or presence of AA. Cells were supplemented with AA (3.5 μ M, 16 h at 37°C) and treated with Erastin (5 μ M, 6 h at 37°C). **(D)** 12-HETE and 15-HETE levels were detected in LGG and GBM cells. Data indicated as mean \pm S.D. (n = 4 experiments). **(E, F)** Acsl4 protein in human glioma (LGG, n = 4; GBM, n = 7) samples was evaluated by western blot and IHC. GAPDH was used as control in western blot assays. **(G)** Database analysis (TCGA, Rembrandt) of different grades of human primary gliomas. Expression of Acsl4 mRNA in LGG (WHO II) was compared to that of GBM (WHO IV). **(H)** Kaplan–Meier survival analysis (TCGA, Rembrandt) of high versus low Acsl4-expressing gliomas. Log-rank test. Scale bars: 50 μ m. *p < 0.05, **p < 0.01, ***p < 0.001.

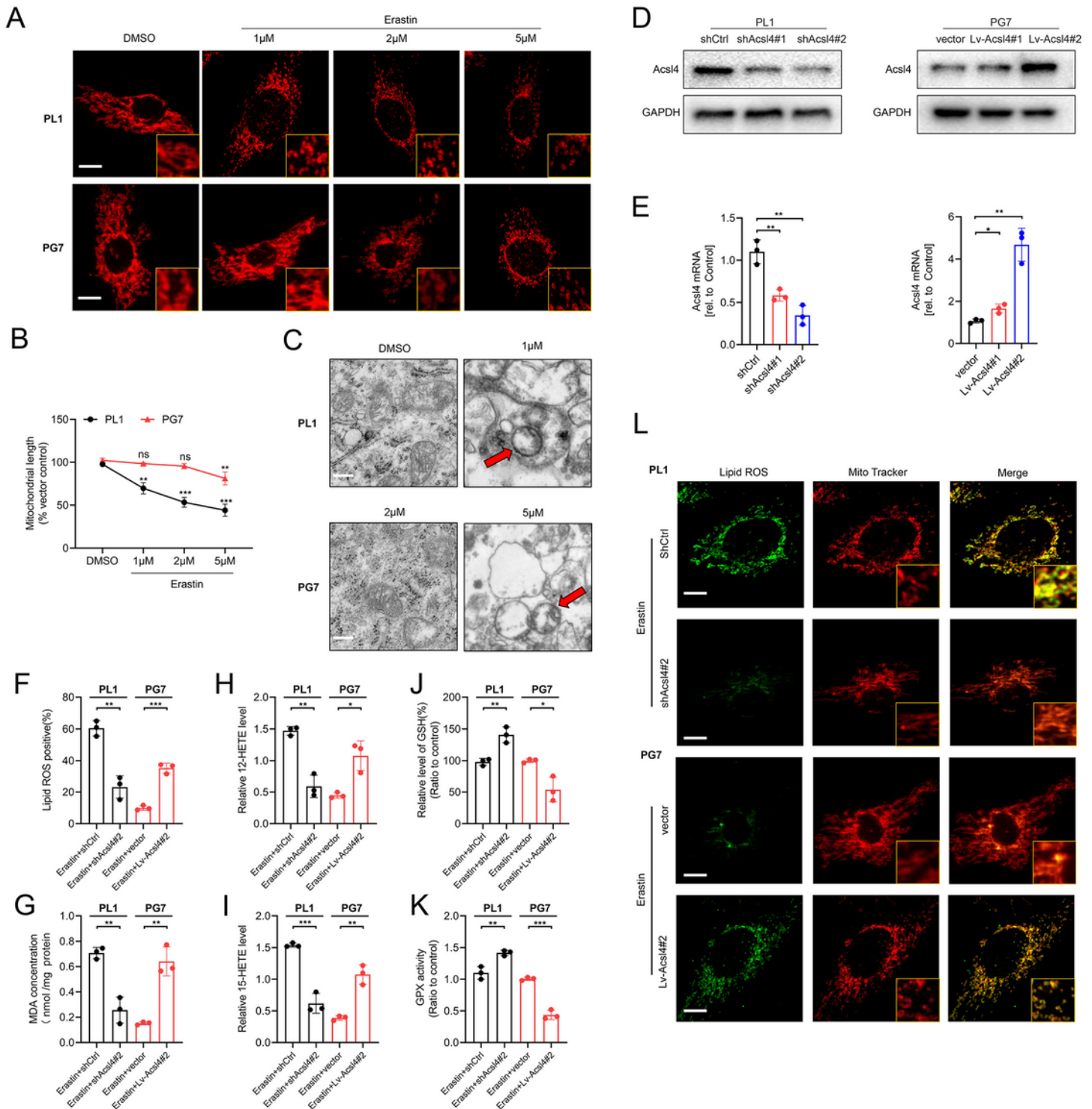


Figure 2

Acs4 participated in mitochondrial-morphology regulation in ferroptosis.

(A) Representative images by immunofluorescence showed mitochondrial morphology in PL1 and PG7 cells treated with Erastin in dose-dependent (6 h). Scale bar: 10 μ m. (B) The mean length of mitochondria in PL1 and PG7 cells treated with Erastin in dose-dependent (6 h). Data indicated as mean \pm S.D. (n = 3

experiments). **(C)** Representative transmission electron microscopy images showed morphology of mitochondria in PL1 and PG7 cells under Erastin treatment(6 h). Mitochondria showed the increased membrane density and shrunken morphology (red arrows). Scale bar: 2 μ m. **(D)** Acsl4 protein expression in Acsl4 shRNA-mediated knockdown PL1 cells and Acsl4 overexpression PG7 cells were determined by western blot. **(E)** Acsl4 mRNA expression in Acsl4 shRNA-mediated knockdown PL1 cells and Acsl4 overexpression PG7 cells were determined by qPCR. Data indicated as mean \pm S.D. (n = 3 experiments). **(F-K)** Intracellular ROS, MDA,12-HETE,15-HETE, GSH and GPX activity in PL1 cells after 1 μ M Erastin treatment and in PG7 cells after 2 μ M Erastin treatment(6 h). Data indicated as mean \pm S.D. (n = 3 experiments). **(L)** Confocal images showed colocalization of oxidized lipid (green) and mitochondria (red). PL1 and PG7 cells were treated as indicated before and then stained with BODIPY C11 and MitoTracker. Scale bar: 10 μ m. *p < 0.05, **p < 0.01, ***p < 0.001.

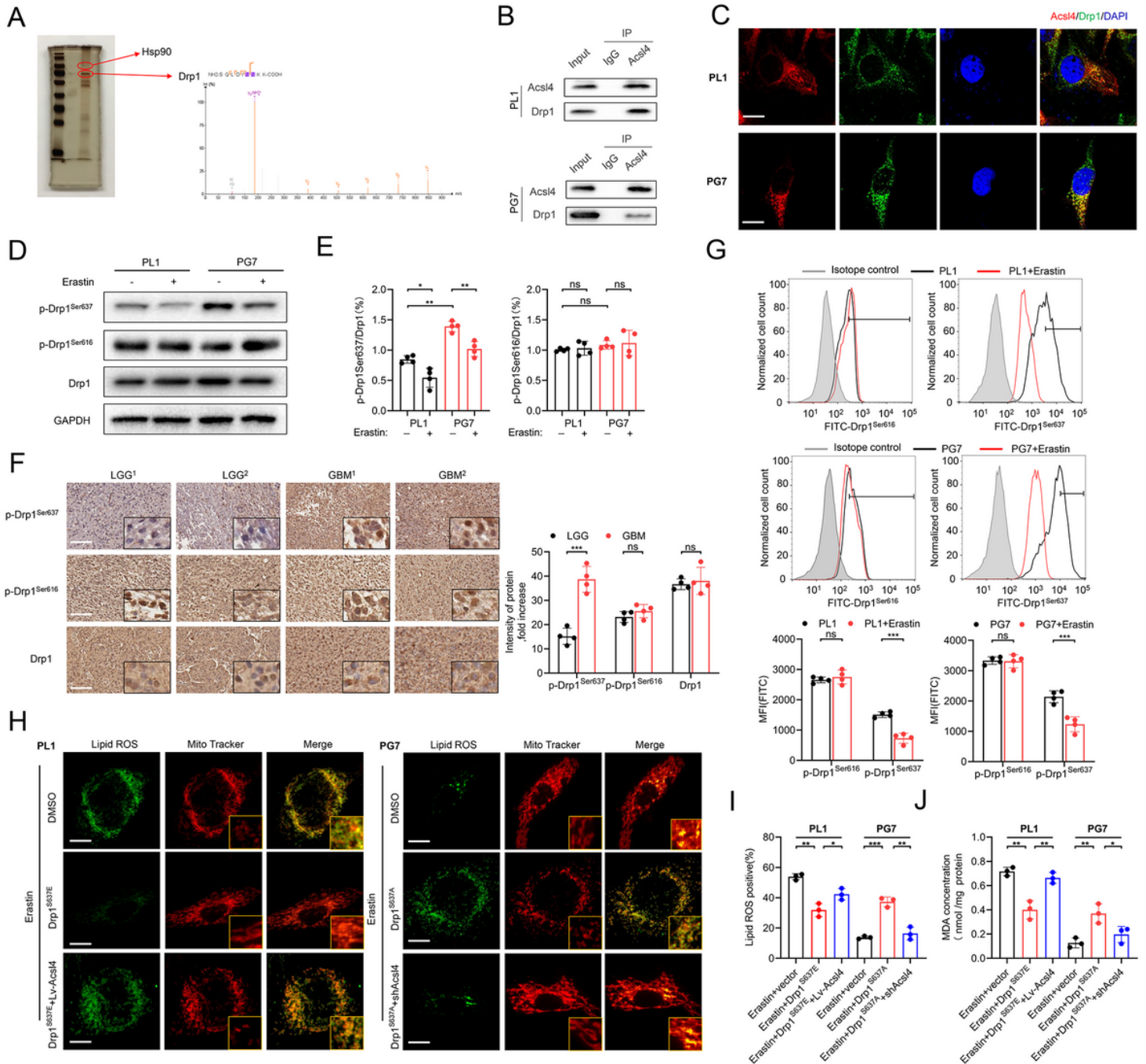


Figure 3

Drp1 phosphorylation was essential for Acsl4-dependent ferroptosis.

(A) SDS-PAGE silver staining showed typical pull-down results of Acsl4 after incubation with PL1 cell lysate. Mass spectrometry identified the band framed in the oval as Drp1. (B) The interaction between Acsl4 and Drp1 was confirmed by co-immunoprecipitation in PL1 and PG7 cells. (C) Confocal images showed colocalization of Acsl4 (red) and Drp1 (green) in PL1 and PG7 cells. Nuclei were counterstained with Hoechst (blue). Scale bars: 10 μm. (D-E) Expression of p-Drp1^{Ser637}, p-Drp1^{Ser616} and Drp1 were determined by western blot in PL1 and PG7 cells in the presence or absence of Erastin (5 μM, 6 h). Drp1

was used as a loading control of two types p-Drp1. GAPDH was used as control. Data indicated as mean \pm S.D. (n = 4 experiments). **(F)** Representative images of IHC staining of p-Drp1^{Ser637}, p-Drp1^{Ser616} and Drp1 in two pairs LGG and GBM tissues. Scale bars: 50 μ m. Data indicated as mean \pm S.D. (n = 4 experiments). **(G)** Flow cytometric analysis of p-Drp1^{Ser637} and p-Drp1^{Ser616} levels in PL1 and PG7 cells. Isotype control was set in gray. The histogram showed mean fluorescence intensity (MFI) values for control and Erastin treated cells. Data indicated as mean \pm S.D. (n = 4 experiments). **(H)** Confocal images showed colocalization of oxidized lipid (green) and mitochondria (red). PL1 cells of indicated groups were treated with Erastin(1 μ M, 6 h) and PG7 cells of indicated groups were treated with Erastin(2 μ M, 6 h), then cells were stained with BODIPY C11 and MitoTracker. Scale bar: 10 μ m. **(I-J)** Intracellular ROS and MDA level in PL1 and PG7 cells treated as indicated before. Data indicated as mean \pm S.D. (n = 3 experiments). *p < 0.05, **p < 0.01, ***p < 0.001.

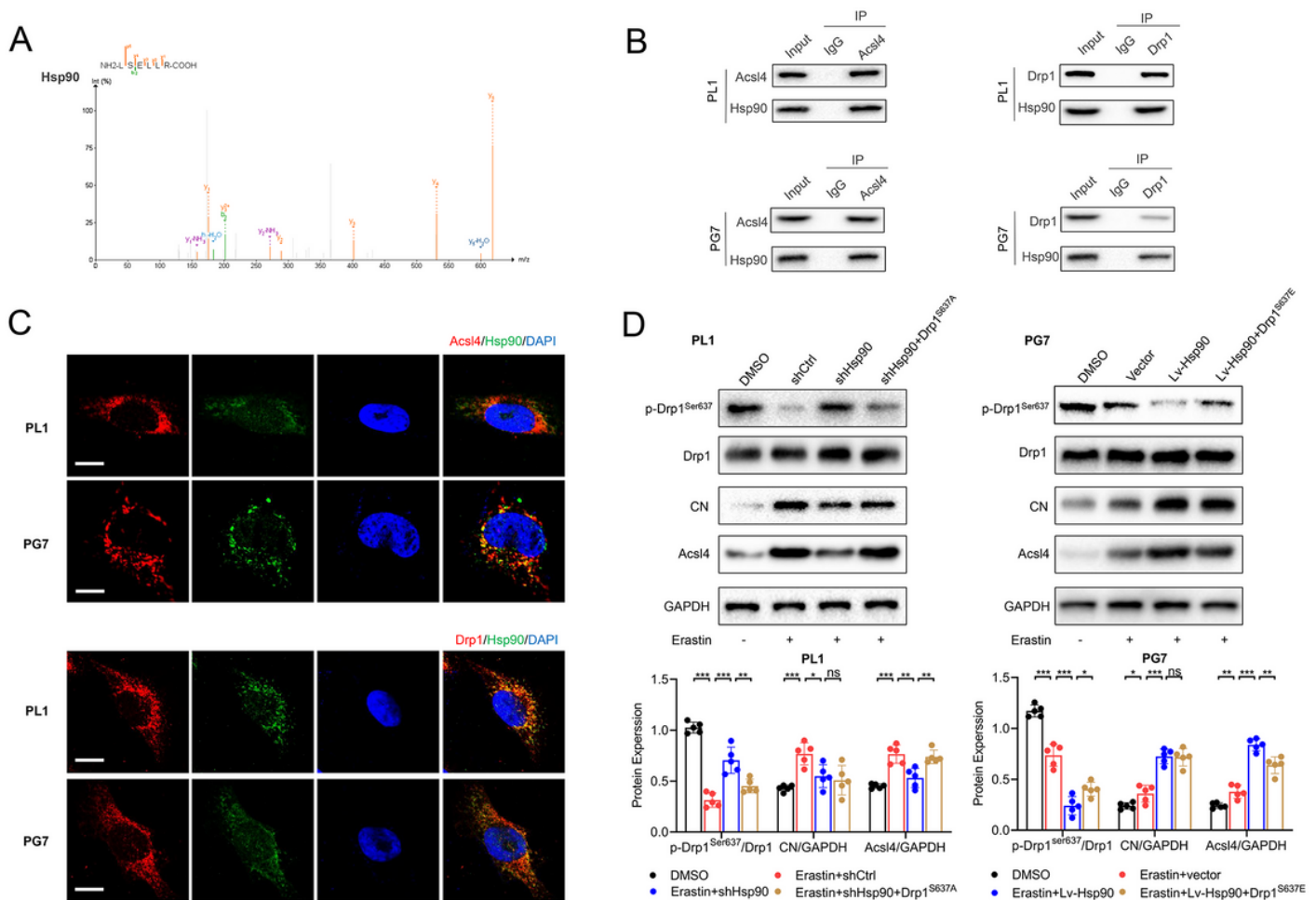
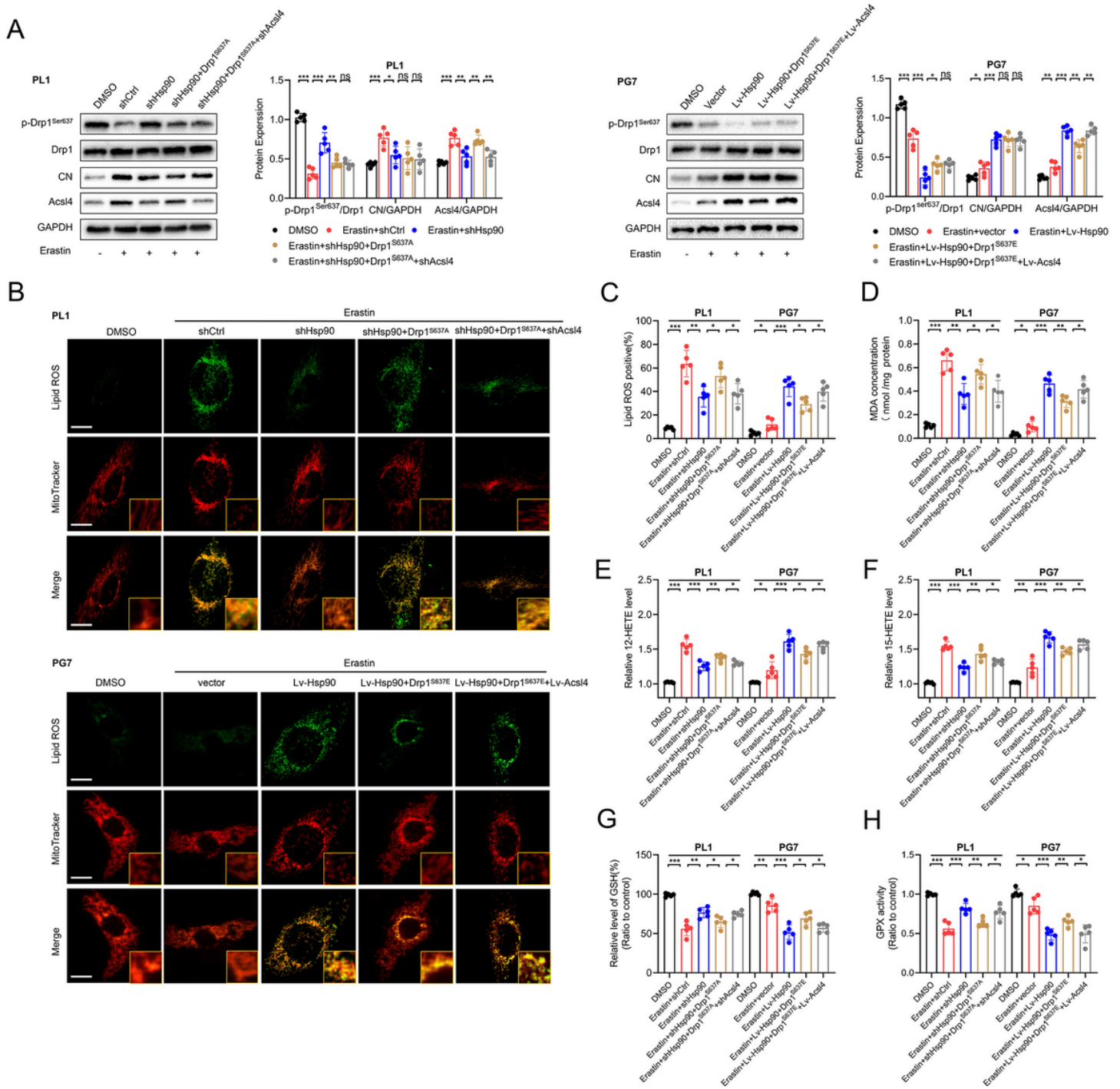


Figure 4

Hsp90 regulated Drp1 phosphorylation via calcineurin in gliomas.

(A) SDS-PAGE silver staining showed typical pull-down results of Acsl4 after incubation with PL1 cell lysate. Mass spectrometry identified the band framed in the oval as Hsp90. **(B)** The interaction between

Acsl4, Drp1 and Hsp90 was confirmed by coimmunoprecipitation in PL1 and PG7 cells. **(C)** Confocal images showed colocalization of Acsl4 (red) and Hsp90(green), Drp1 (red) and Hsp90(green) in PL1 and PG7 cells. Nuclei were counterstained with Hoechst (blue). Scale bars: 10 μ m. **(D)** Expressions of proteins in Hsp90-Acsl4 pathway were determined by western blot in indicated groups. Data indicated as mean \pm S.D. (n = 5 experiments). *p < 0.05, **p < 0.01, ***p < 0.001.



(A) Expressions of proteins in Hsp90-Acs14 pathway were determined by western blot in indicated groups. Data indicated as mean \pm S.D. (n = 5 experiments). **(B)** Confocal images showed colocalization of oxidized lipid (green) and mitochondria (red). PL1 cells of indicated groups were treated with Erastin(1 μ M, 6 h) and PG7 cells of indicated groups were treated with Erastin(2 μ M, 6 h), then cells were stained with BODIPY C11 and MitoTracker. Scale bar: 10 μ m. **(C-H)** Intracellular ROS,MDA,12-HETE,15-HETE level, GSH and GPX activity in in PL1 and PG7 cells treated as indicated before. Data indicated as mean \pm S.D. (n = 5 experiments). *p < 0.05, **p < 0.01, ***p < 0.001.

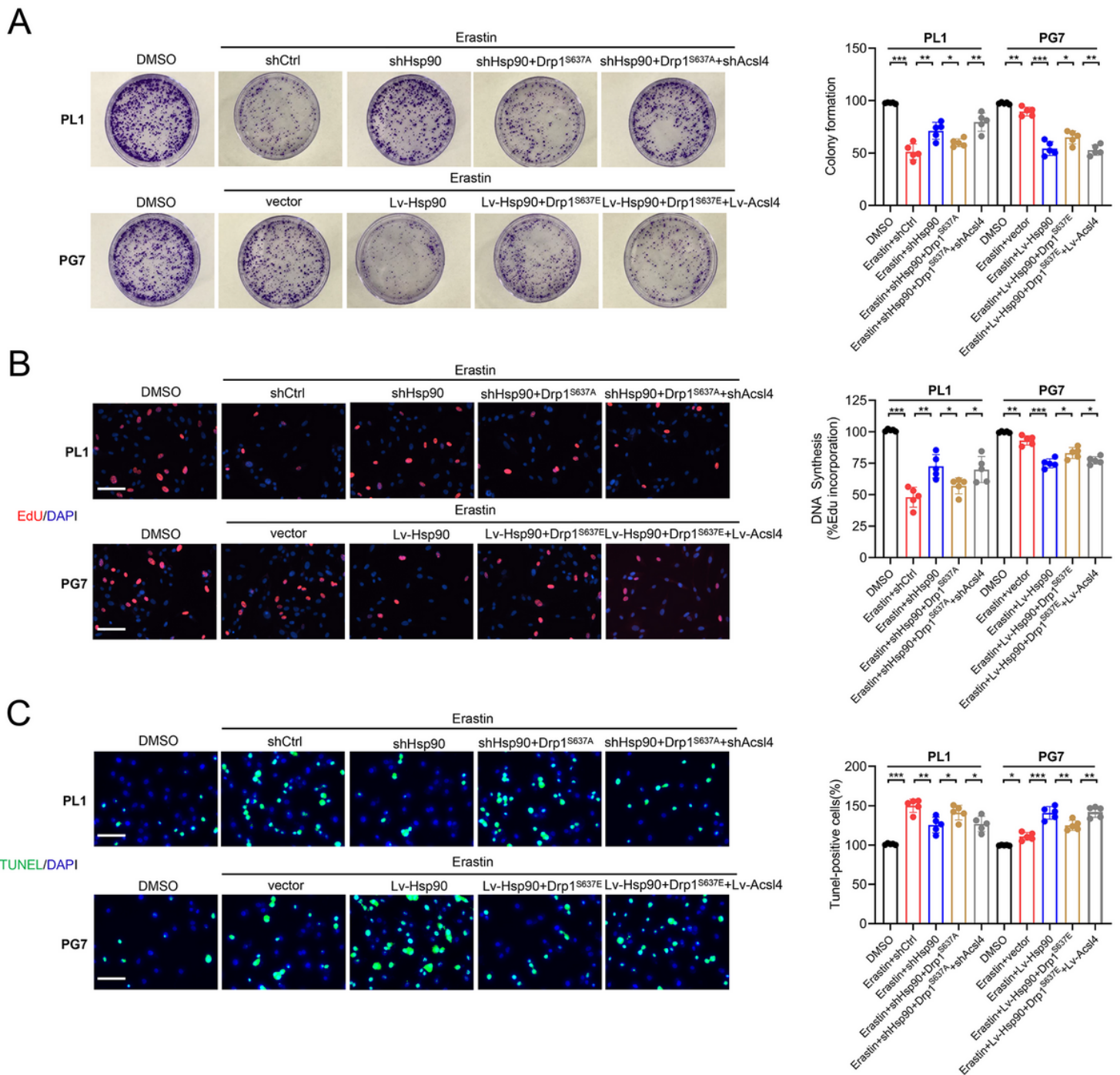


Figure 6

Promotion of the Hsp90-Acs14 pathway enhanced Erastin sensitivity in vitro.

(A) Colony formation assays in indicated groups in PL1 cells after 1 μ M Erastin treatment and in PG7 cells after 2 μ M Erastin treatment (6 h). Data indicated as mean \pm S.D. (n = 5 experiments). (B) EdU assays. Scale bar: 50 μ m. Data indicated as mean \pm S.D. (n = 5 experiments). (C) TUNEL assays. Scale bar: 50 μ m. Data indicated as mean \pm S.D. (n = 5 experiments). *p < 0.05, **p < 0.01, ***p < 0.001.

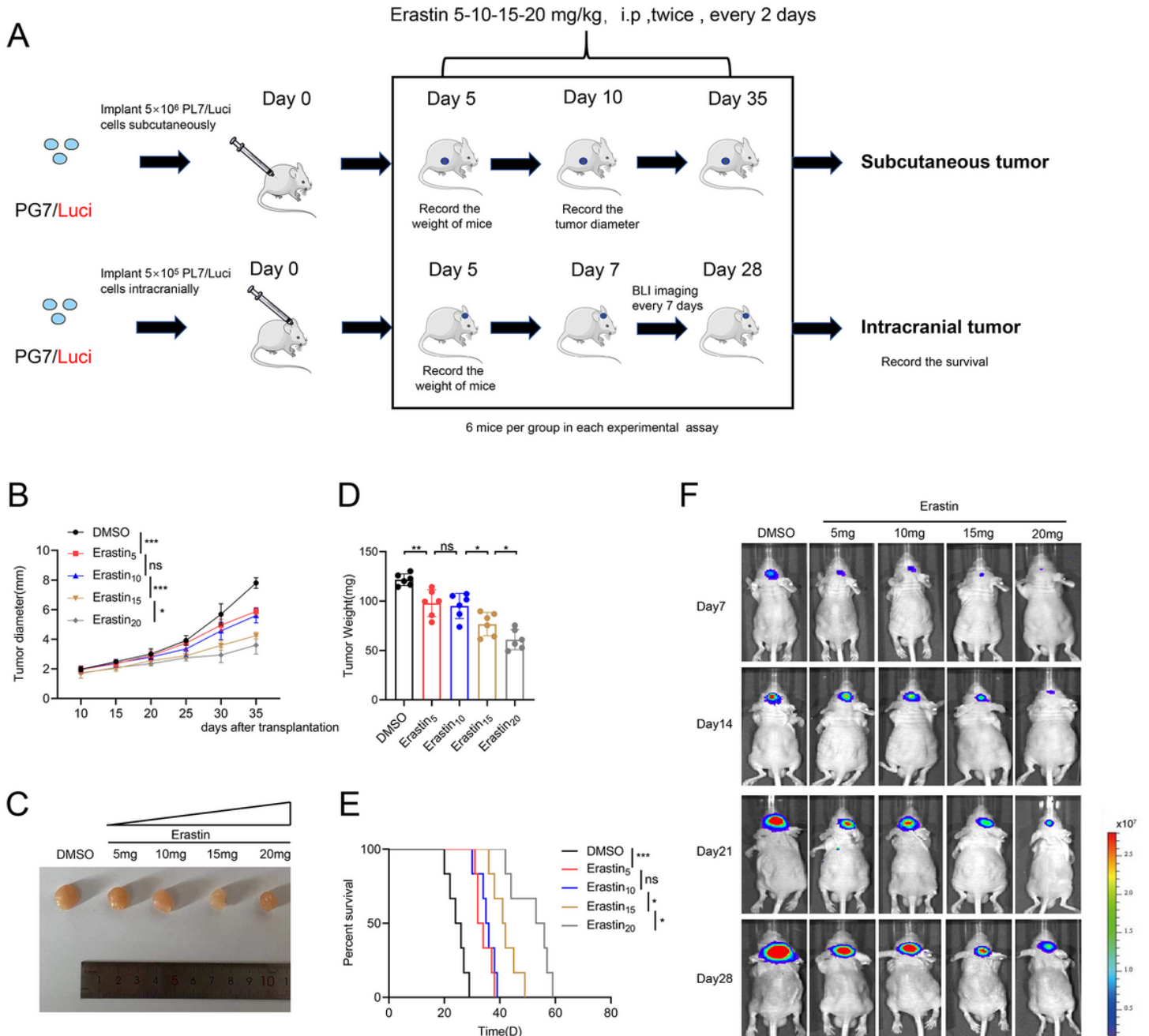


Figure 7

Erastin inhibited glioblastoma growth in vivo.

(A) Mice were subcutaneously and intracranially xenografted with PG7 cells ($5 \times 10^6/5 \times 10^5$ cells) and treated intraperitoneally with Erastin ($5\text{-}10\text{-}15\text{-}20 \text{ mg kg}^{-1} \text{ day}^{-1}$ per mouse) or DMSO (0.3%) twice, every 2 days. **(B)** Diameter of subcutaneous tumors. Data indicated as mean \pm S.D. ($n = 6$ mice per group). **(C)** Image of subcutaneous tumors treated with different concentrations of Erastin. **(D)** Weight of subcutaneous tumors. Data indicated as mean \pm S.D. ($n = 6$ mice per group). **(E)** Kaplan–Meier survival of mice. ($n = 6$ mice per group). **(F)** Bioluminescence imaging was performed on Days 7, 14, 21 and 28 days after implantation. * $p < 0.05$, ** $p < 0.01$, *** $p < 0.001$.

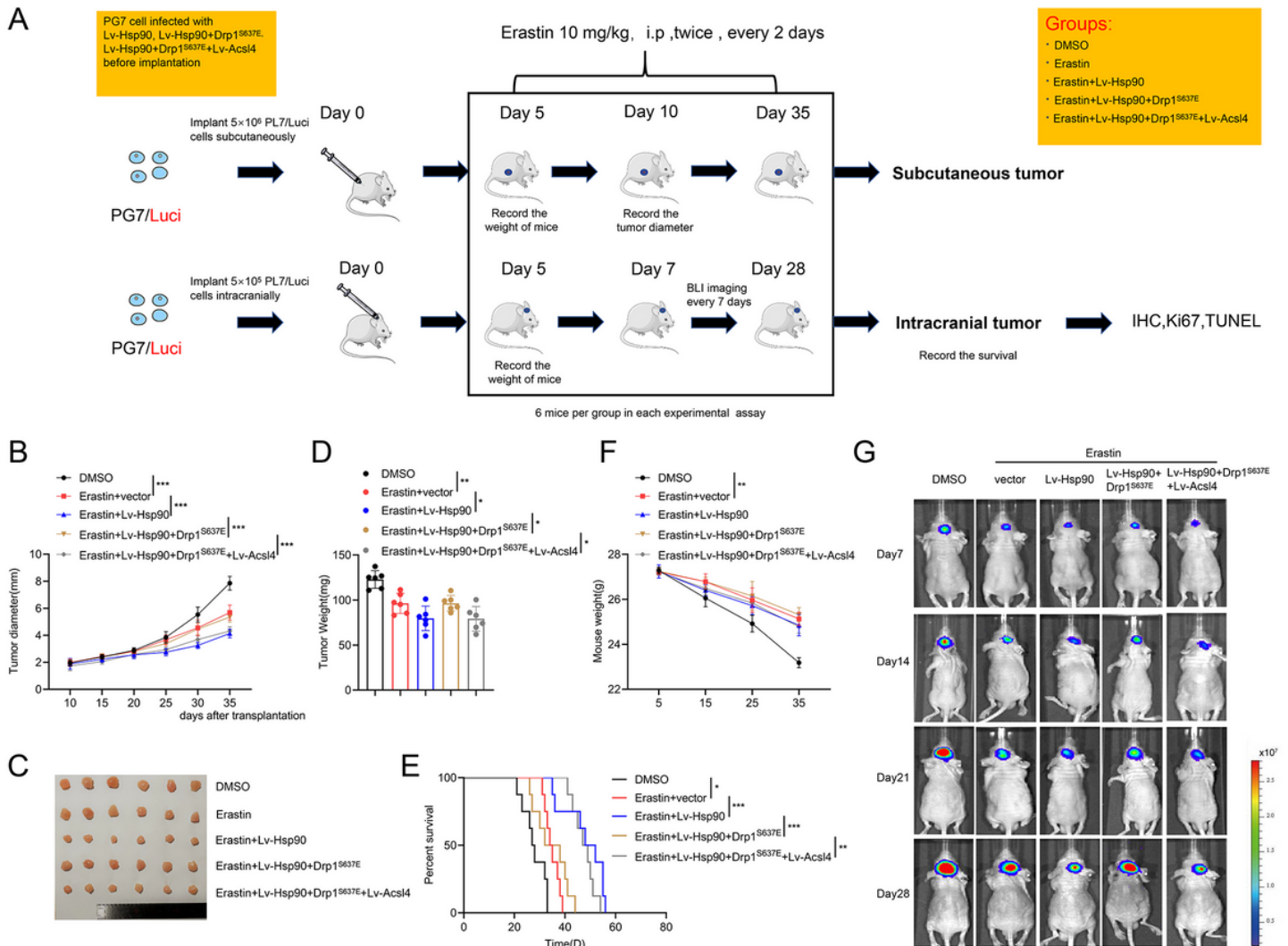


Figure 8

Promotion of the Hsp90-Acs14 pathway enhanced Erastin sensitivity in vivo.

(A) Mice were subcutaneously and intracranially xenografted with PG7 cells of different groups ($5 \times 10^6/5 \times 10^5$ cells) and treated intraperitoneally with Erastin ($10 \text{ mg kg}^{-1} \text{ day}^{-1}$ per mouse) or DMSO (0.3%) twice, every 2 days. **(B)** Diameter of subcutaneous tumors. Data indicated as mean \pm S.D. ($n = 6$ mice per group). **(C)** Image of subcutaneous tumors. **(D)** Tumor weight of subcutaneous tumors. Data are indicated as mean \pm S.D. ($n = 6$ mice per group). **(E)** Kaplan–Meier survival of mice. ($n = 6$ mice per group).

group). **(F)** Weight of mice during the experiment. Data indicated as mean \pm S.D. (n = 6 mice per group). **(G)** Bioluminescence imaging was performed on Days 7, 14, 21 and 28 days after implantation. *p < 0.05, **p < 0.01, ***p < 0.001.

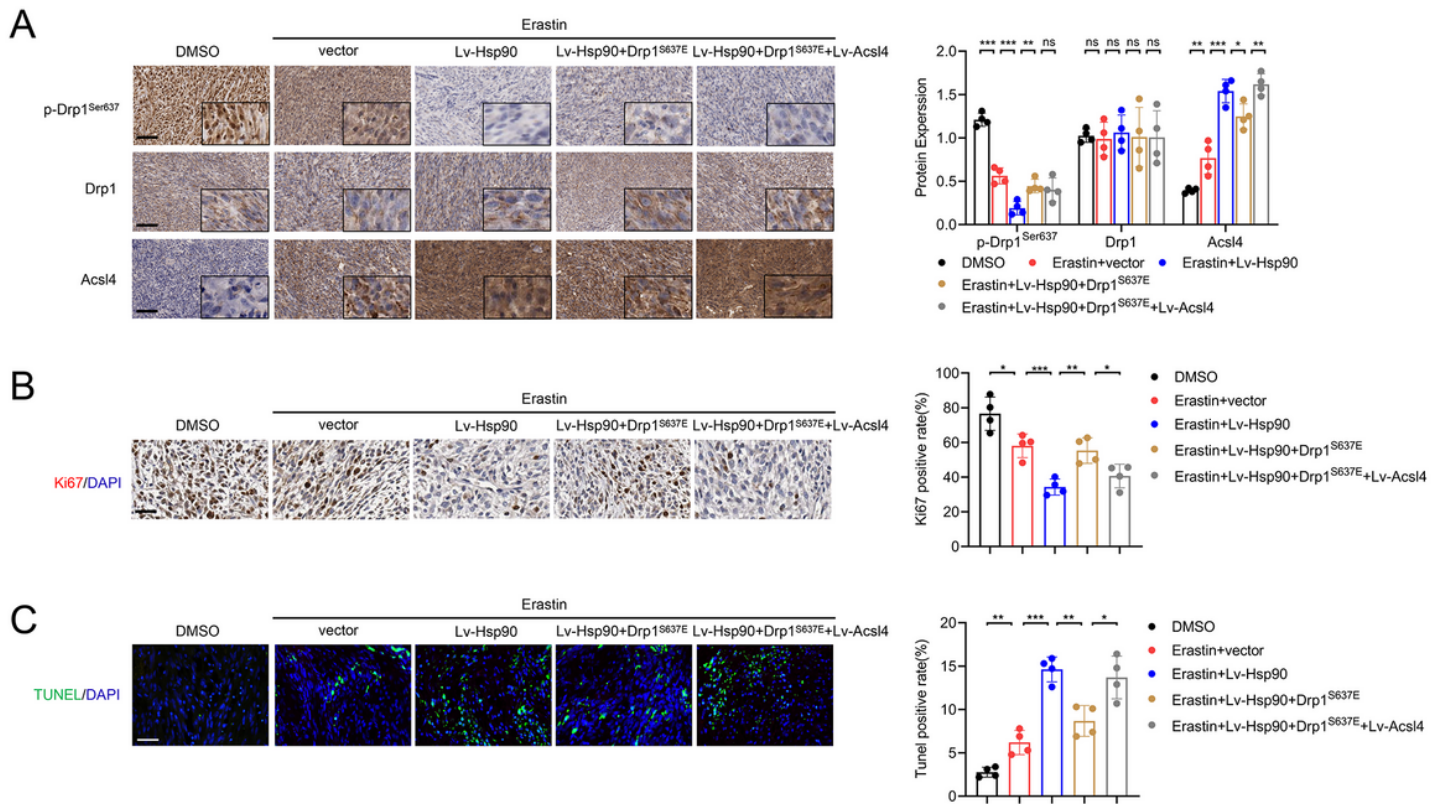


Figure 9

Promotion of the Hsp90-Acsl4 pathway enhanced Erastin sensitivity in vivo.

(A) IHC assay for p-Drp1^{Ser637}, Drp1 and Acsl4. Scale bar: 50 μ m. Data indicated as mean \pm S.D. (n = 4 mice per group). **(B)** IHC assay for Ki67. Scale bar: 50 μ m. Data indicated as mean \pm S.D. (n = 4 mice per group). **(C)** TUNEL assay. Scale bar: 50 μ m. Data indicated as mean \pm S.D. (n = 4 mice per group). *p < 0.05, **p < 0.01, ***p < 0.001.

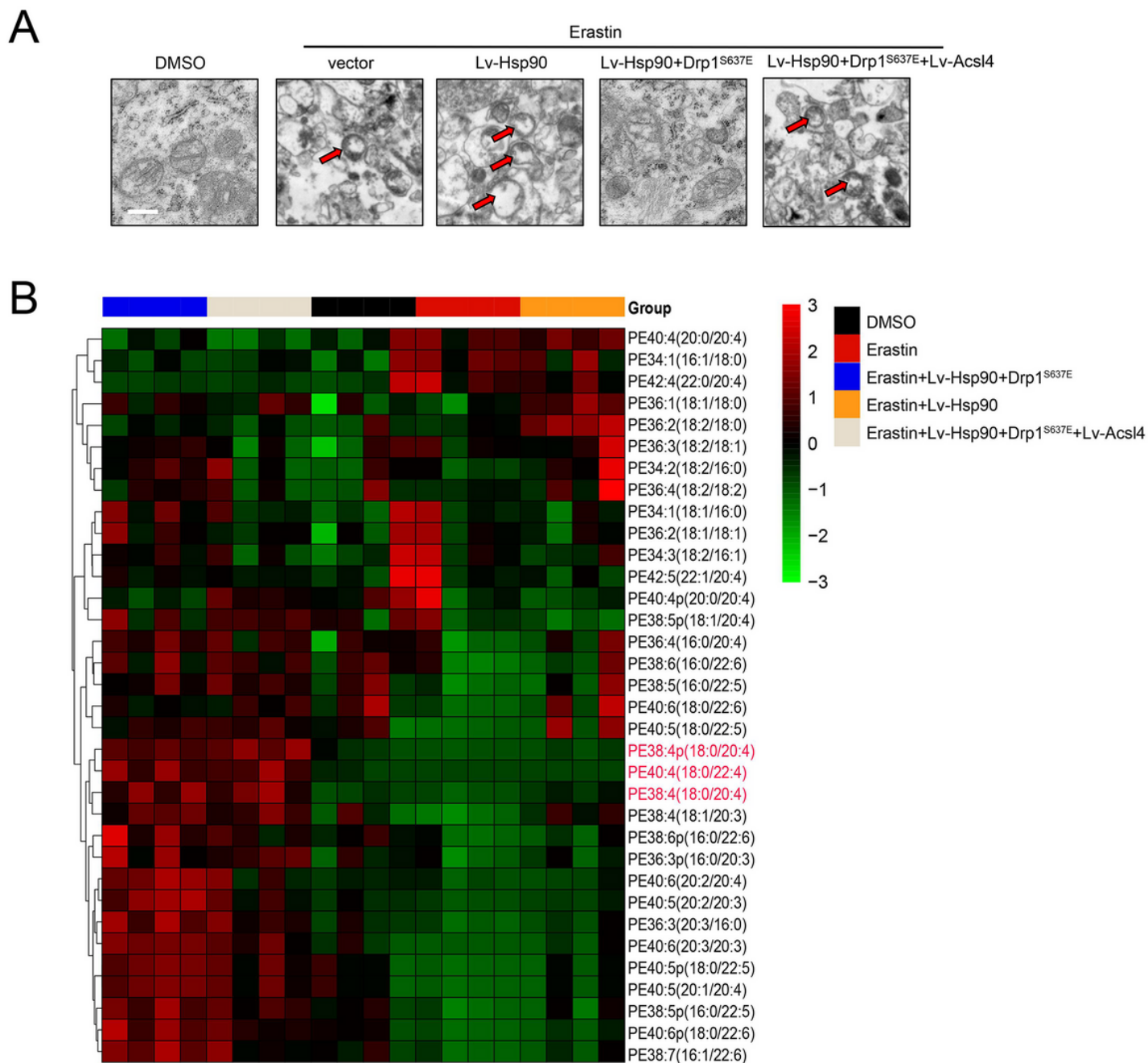


Figure 10

Promotion of the Hsp90-Acsl4 pathway enhanced Erastin sensitivity in vivo.

(A) Representative transmission electron microscopy images revealed mitochondrial morphology of different groups. Scale bar: 1 μ m. **(B)** Heatmap of all major PE species with hierarchical clustering of the groups DMSO, Erastin, Erastin+Lv-Hsp90, Erastin

+Lv-Hsp90+Drp1^{S637E}, Erastin+Lv-Hsp90+Drp1^{S637E}+Lv-Acsl4.

Supplementary Files

This is a list of supplementary files associated with this preprint. Click to download.

- [Supplement.docx](#)
- [GraphicalAbstract.tif](#)